

Thalamic bursting and the role of timing and synchrony in thalamocortical signaling in the awake mouse

Highlights

- Optogenetic thalamic hyperpolarization enhances thalamic sensory-evoked bursting
- S1 cortical responses are not amplified
- Thalamic bursting increases S1 timing precision and synchrony
- A highly sensitive, timing-based gating of sensory signaling to cortex

Authors

Peter Y. Borden, Nathaniel C. Wright, Arthur E. Morrissette, Dieter Jaeger, Bilal Haider, Garrett B. Stanley

Correspondence

garrett.stanley@bme.gatech.edu

In brief

It has long been proposed that the thalamus serves as a dynamic gate for control of sensory signaling to cortex through switching between tonic and burst firing modes. Using optogenetic manipulation in the awake mouse, Borden et al. demonstrate a thalamic burst-driven, timing-based gating of sensory signaling to the cortex.



Article

Thalamic bursting and the role of timing and synchrony in thalamocortical signaling in the awake mouse

Peter Y. Borden,^{1,3,4} Nathaniel C. Wright,^{1,3} Arthur E. Morrissette,^{2,5} Dieter Jaeger,² Bilal Haider,¹ and Garrett B. Stanley^{1,6,*}

¹Wallace H Coulter Department of Biomedical Engineering, Georgia Institute of Technology, Emory University, Atlanta, GA 30332, USA

²Emory University, Department of Biology, Atlanta, GA 30322, USA

³These authors contributed equally

⁴Present address: AbbVie, Chicago, IL 60064, USA

⁵Present address: SkinIO, Chicago, IL 60607, USA

⁶Lead contact

*Correspondence: garrett.stanley@bme.gatech.edu

<https://doi.org/10.1016/j.neuron.2022.06.008>

SUMMARY

The thalamus controls transmission of sensory signals from periphery to cortex, ultimately shaping perception. Despite this significant role, dynamic thalamic gating and the consequences for downstream cortical sensory representations have not been well studied in the awake brain. We optogenetically modulated the ventro-posterior-medial thalamus in the vibrissa pathway of the awake mouse and measured spiking activity in the thalamus and activity in primary somatosensory cortex (S1) using extracellular electrophysiology and genetically encoded voltage imaging. Thalamic hyperpolarization significantly enhanced thalamic sensory-evoked bursting; however, surprisingly, the S1 cortical response was not amplified, but instead, timing precision was significantly increased, spatial activation more focused, and there was an increased synchronization of cortical inhibitory neurons. A thalamocortical network model implicates the modulation of precise timing of feedforward thalamic population spiking, presenting a highly sensitive, timing-based gating of sensory signaling to the cortex.

INTRODUCTION

We explore the world through our sensory periphery, where sensors transduce the signals that ultimately give us perception of the world. The mammalian sensory thalamus gates information from the periphery to primary sensory cortices, controlling what signals do and do not make their way to cortex, thus playing a very critical role in sensing. Far from a static relay, the thalamus is under continuous influence by modulatory inputs from brainstem and feedback mechanisms from cortex (Sherman and Guillery, 2002; Sherman, 2005), most extensively explored in the context of sleep and epileptic seizures (Huguenard and McCormick, 2007; Fogerson and Huguenard, 2016). The large majority of detailed thalamic studies focusing on its potential role in sensory signaling have been either in *ex-vivo*/slice preparations or in intact/*in-vivo* preparations under anesthesia, where prominent thalamic properties such as synchronization of convergent thalamocortical (TC) projections and tonic/burst gating have been shown to strongly boost signaling under these conditions (Sherman, 2001a; Sherman, 2001b; Swadlow and Gusev, 2001; Swadlow, 2002; Lesica and Stanley, 2004; Lesica et al., 2006; Wang et al., 2010; Stanley et al., 2012; Whitmire et al.,

2016). Recent studies exploring the role of thalamus in the awake, unanesthetized brain have confirmed the critical role of thalamus in grossly modulating sensory cortex (Halassa et al., 2011; Poulet et al., 2012; Lewis et al., 2015; Reinhold et al., 2015; Yu et al., 2016; Wright et al., 2021). However, whether increases in thalamic excitability act to boost cortical sensory-evoked responses in the awake brain as predicted from *ex-vivo* and anesthetized studies is unknown.

Serving as the primary input to sensory cortex, properties of thalamic activity strongly shape the spontaneous, baseline activity of cortex, as well as the corresponding cortical response to ascending sensory inputs. It has been shown that even small changes in baseline membrane potential have appreciable effects on spontaneous firing of thalamic neurons (Béhuret et al., 2015), setting the overall tone of synaptic drive to cortex. The use of pharmacology to directly modulate thalamus (Godwin et al., 1996; Hirata and Castro-Alamancos, 2010; Poulet et al., 2012) or opto/microstimulation and pharmacology to indirectly affect thalamus through cortical (Olsen et al., 2012; Mease et al., 2014; Crandall et al., 2015; Li and Ebner, 2016; Kirchgessner et al., 2020) and subcortical (Aguilar and Castro-Alamancos, 2005) inputs has further causally revealed the extreme sensitivity



of cortex to overall thalamic drive. One prominent characteristic of neurons in the thalamus is the presence of T-type calcium channels that are normally inactivated but become de-inactivated through prolonged hyperpolarization (Jahnsen and Llinás, 1984a, 1984b; Sherman and Koch, 1986; Suzuki and Rogawski, 1989). Subsequent depolarizing inputs lead to calcium-mediated “bursts” of action potentials characterized by transient, high-frequency spiking, which is distinct from “tonic” spiking mediated through Na^+/K^+ channel dynamics. Most actively investigated in the context of sleep states and rhythmic discharge, the role of this mechanism in sensory signaling remains unclear, despite decades of speculation. At the synaptic level, TC high-frequency bursting events have been shown to have a significant impact on downstream cortical activation (Swadlow and Gusev, 2001), where thalamic bursts are associated with an amplified post-synaptic response in recipient cortical neurons, thought to arise primarily from properties of the TC synapse. Coupled with sensitivity of cortex to the timing of thalamic inputs via the “window of opportunity” established by the disinaptic feedforward cortical inhibition (Pinto et al., 2000, 2003; Wehr and Zador, 2003; Wilent and Contreras, 2004, 2005; Gabernet et al., 2005; Isaacson and Scanziani, 2011), the gating of thalamic signaling through the aggregate effects of all these properties across the thalamic population is hypothesized to serve a critical role in processing sensory information (Crick, 1984; Pinto et al., 2000; Sherman and Guillery, 2002; Wilent and Contreras, 2004; Sherman, 2005). However, this has not been investigated extensively in the intact brain due to the lack of methodological approaches to precisely measure and manipulate thalamic properties. To date, no studies have utilized temporally precise, repeatable, and reversible modulation to precisely measure the effects of thalamic burst/tonic gating in awake cortex at the level of population signals and single-neuron firing.

Here, we directly determined how thalamic gating properties control sensory-evoked thalamic and cortical responses in the vibrissa pathway of the awake, head-fixed mouse. Instead of driving or silencing neural activity, optogenetic manipulation was used to modulate thalamus while recording extracellular thalamic and cortical activity and acquiring wide-field cortical voltage imaging, using the voltage indicator ArcLight (Jin et al., 2012; Borden et al., 2017). We found that baseline thalamic firing rate at steady state was surprisingly invariant to optogenetic thalamic hyperpolarization through a transition from tonic to burst firing activity, and the baseline activity in S1 cortex at steady state was correspondingly invariant to thalamic hyperpolarization, following a brief transient increase in firing activity. In response to sensory stimuli, the thalamic hyperpolarization significantly enhanced the sensory-evoked thalamic bursting; however, the magnitude of the response in S1 cortex was not amplified but instead slightly attenuated relative to baseline, despite the burst-dominated thalamic input. Notably, the sensory-evoked response was also significantly more brief and spatially focused and accompanied by an increase in the synchronization of the putative cortical fast-spiking (FS) inhibitory neurons. A TC network model replicated these findings and implicated changes in the precise timing and synchronization across the thalamic population as a likely mechanism underlying the experimental observations. Taken together, the results here

point to timing rather than response magnitude as a fundamental feature of the TC circuit, presenting a dynamic, timing-based gating of sensory signaling to cortex.

RESULTS

All experiments were conducted in the vibrissa pathway of the mouse (Figure 1A). To directly test the predictions of previous *in-vitro* and anesthetized work, we conducted the first experiment in the isoflurane-anesthetized mouse (illustrated in Figure 1B). We utilized extracellular electrodes to record whisker-evoked spiking activity in ventral posterior-medial (VPM) thalamus in the presence (light-emitting diode, LED) and absence (control) of a hyperpolarizing optogenetic modulation of excitatory thalamic relay neurons expressing halorhodopsin (eNphR3.0 [Gradinaru et al., 2010]; see Figure S1), through a small fiber optic cable attached to the electrode (Figure 1B). We used a range of relatively low light levels to induce sustained hyperpolarization, where light levels were in a range that has been previously shown to not induce significant heating of the surrounding tissue (see figure caption and STAR Methods). Control experiments indicate that there was no effect of the light alone in the absence of opsin expression (Figure S4).

Neurons in VPM thalamus responded to a single, computer-controlled punctate whisker stimulation ($1,200^\circ/\text{s}$, sawtooth waveform) with a transient sequence of action potentials (Figure 1D; see STAR Methods). Optogenetic thalamic hyperpolarization significantly increased the sensory-evoked thalamic bursting (Figure 1D), where burst spiking was defined as in Figure 1C. Overall, there was an increase in the evoked response from the Control to the LED condition (Figure 1E left, black), in large part driven by the increase in sensory-evoked thalamic bursting (Figure 1E left, red). In a subset of experiments, we recorded the downstream cortical multiunit (MU) activity (Figure 1E right) and found a corresponding enhanced response in the LED condition. Additionally, we simultaneously recorded cortical S1 activation at a meso-scopic scale with optical voltage imaging in primary somatosensory (barrel) cortex using a genetically encoded voltage indicator (GEVI, ArcLight, Borden et al., 2017; see STAR Methods and Figure S4), which confirmed a corresponding amplification of the S1 sensory-evoked response during thalamic hyperpolarization (Figures 1F and 1G). Note that the convention used throughout the analyses here is to present the negative of the fluorescence measure, such that an increase in neural activity corresponds to a positive change in the fluorescence measure. There was an amplification in the peak response, followed by a gradual return to baseline over approximately ~ 200 ms. This induced amplification of the peak cortical sensory response is consistent with the enhanced VPM sensory response, as predicted by previous observations of spontaneous thalamic bursting and the impact on downstream synaptic targets in cortical layer 4 (Swadlow and Gusev, 2001).

Thalamic hyperpolarization and ongoing thalamic and cortical activity in the awake brain

In a next set of experiments, we sought to characterize the influence of thalamic properties on gating of signaling to cortex in the awake mouse. Before turning to the sensory-evoked responses,

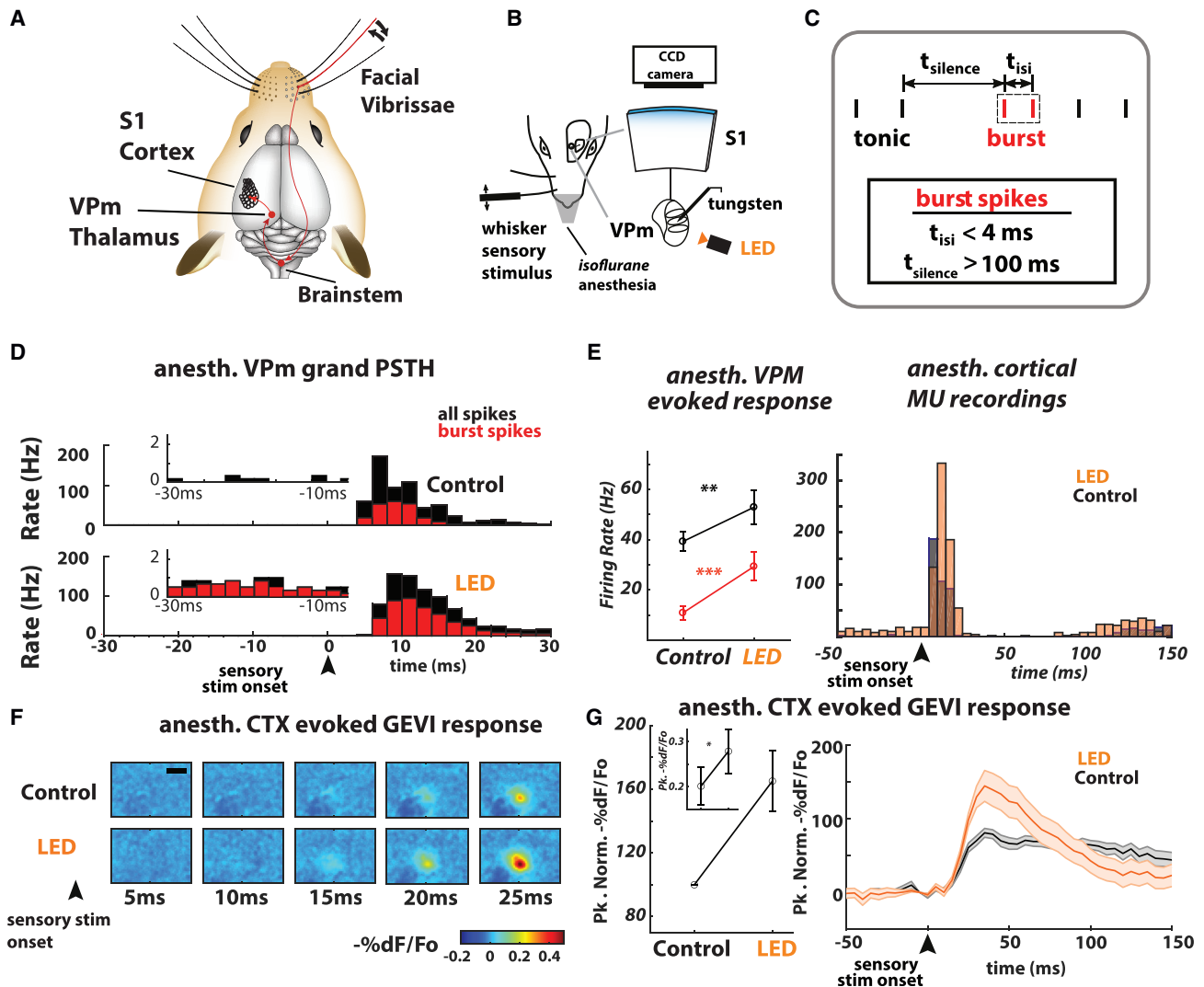


Figure 1. Thalamic hyperpolarization amplifies thalamic bursting and sensory-evoked cortical response in the anesthetized mouse

(A) Pathway of the mouse vibrissa system from the facial vibrissae in the periphery, to brainstem, to thalamus, and to S1.

(B) Experimental setup. Mice were injected with the viral vector eNphR3.0 (AAV5-CamIIKiasne-eNphR3.0-mCherry) targeting the ventral posterior-medial (VPM) region of the thalamus and the viral vector ArcLight (AAV1-hyns1-ArcLightD-SV40) in the vibrissa region of the primary somatosensory cortex (S1). For optogenetic hyperpolarization, thalamic units were presented with constant illumination (LED, 590 nm, approx. 17 mW/mm²) from a 200- μ m optic fiber, with LED illumination starting at 0.5 s preceding stimulus ($t = -0.5$ s) and ending 0.5 s after stimulus ($t = 0.5$ s) while recording simultaneously with a single tungsten electrode.

(C) Thalamic bursts were identified as two or more spikes with inter-spike interval (ISI) less than 4 ms, preceded by silence for 100 ms or more. Thalamic spikes that were part of an identified burst were classified as putative burst spikes (red), and all else were classified as tonic spikes (black).

(D) Peri-stimulus time histogram (PSTH) for thalamic spiking in response to a single, punctate whisker stimulus ($t = 0$) for the control (no light, top panel) and thalamic hyperpolarized (LED, bottom panel) conditions, 29 units. Instantaneous firing rates (bin size 2 ms) shown for all spikes (black) and putative burst spikes (red).

(E) (Left) Mean sensory-evoked thalamic firing rate ($n = 29$ thalamic units) over the 0–30 ms time window increased from the control (no light) to the LED conditions, for all spikes (black, $p = 0.0046$, paired Wilcoxon signed-rank test) and burst spikes (red, $p = 4.5 \times 10^{-4}$, paired Wilcoxon signed-rank test). Error bars represent mean \pm SEM. (Right) Mean sensory-evoked cortical multiunit (MU) firing rate from 102 trials (across 2 recordings, 1 mouse, 5-ms bin size).

(F) Example session of GEVI imaging following the delivery of a punctate whisker stimulus at time $t = 0$, for the control (no light, top row) and LED (bottom row) conditions. Images are averaged across 51 trials. Black bar represents 1 mm.

(G) (Left) Mean normalized peak GEVI sensory-evoked response was larger for the LED compared with the control condition ($n = 9$ mice, 13 recording sessions). For this plot, animals and sessions were each normalized to their control levels, and the LED condition is reported relative to the control. (Left inset) Raw relative peak evoked $\%dF/F_0$, $p = 0.017$, paired Wilcoxon signed-rank test, $n = 13$ recordings across 9 mice. (Right) Time series of the normalized sensory-evoked GEVI signal, generated from the integrated fluorescence within the 0.2×0.2 mm ROI in the control (gray) and LED (orange) conditions. Error bars represent mean \pm SEM.

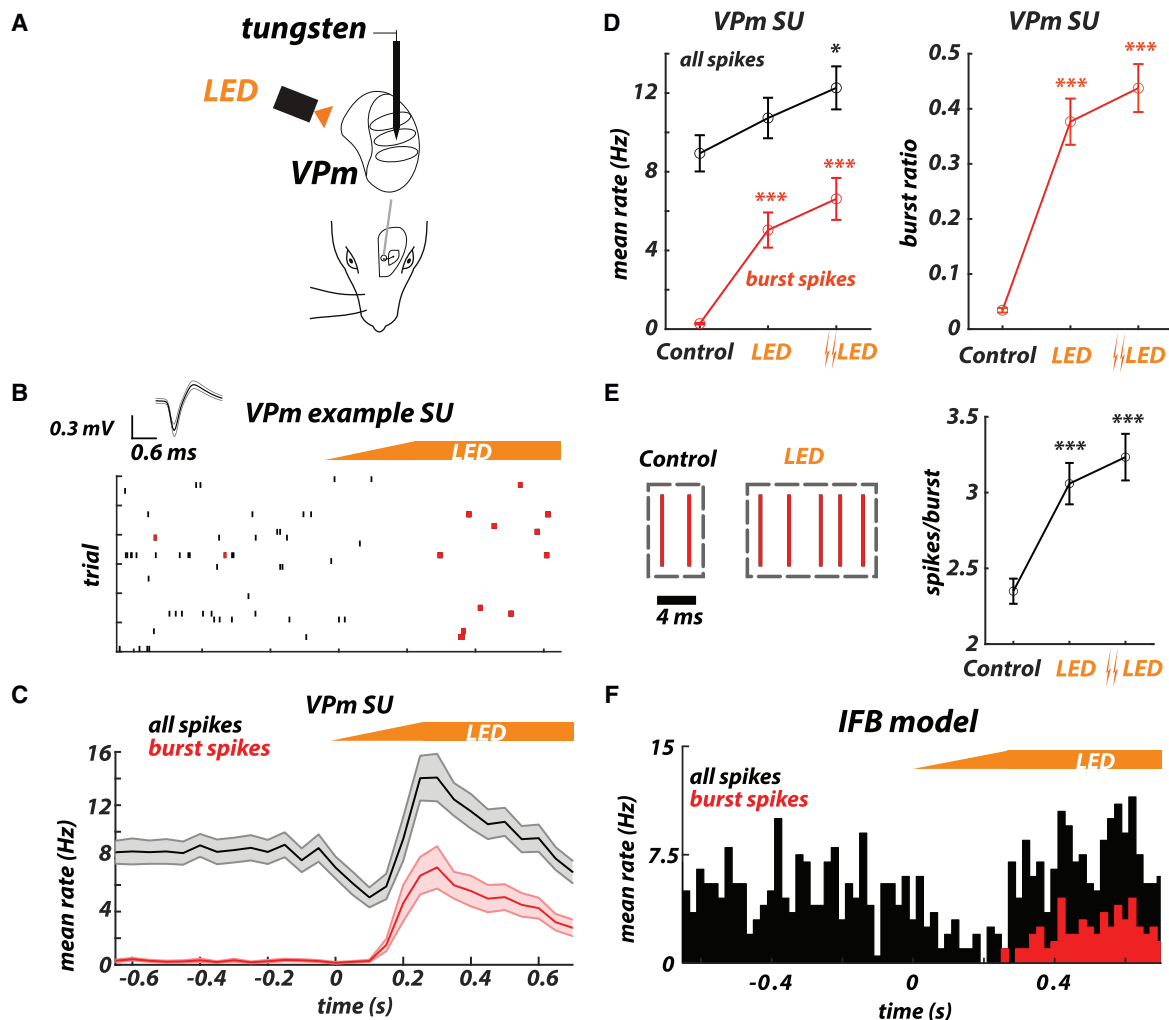


Figure 2. Thalamus baseline firing rate is invariant to optogenetic hyperpolarization via a tonic/burst switch

(A) Experimental setup. Mice were injected with the viral vector eNphR3.0 (AAV5-CamIIKiasne-eNphR3.0-mCherry) targeting the ventral posterior-medial (VPm) region of the thalamus. On each trial, thalamic units were presented with light for 1.5 s (590 nm, LED approx. 17 mW/mm² ramp, Double LED approx. 35 mW/mm² ramp—see STAR Methods) from a 200- μ m optic fiber and recorded simultaneously with a single tungsten electrode.

(B) Example extracellular single trial rasters depicting effects of thalamic hyperpolarization on spiking in VPm thalamus. Black indicates tonic spikes; red indicates burst spikes. Recorded spike waveform shown at top.

(C) Aggregate single-unit (SU, $n = 51$ units) PSTH for all spikes (black) and burst spikes (red). Apparent is an initial decrease in overall firing rate following presentation of light, followed by an increase and a subsequent return to the pre-hyperpolarization level. Bands represent mean \pm SEM.

(D) (Left) Mean single-unit thalamic firing rate over the 250–750 ms time window from the control (no light) to the LED condition, for all spikes (black, Control versus LED $p = 0.2$, control versus Double LED $p = 0.02$, unpaired two-sample t test, $n = 54$ for control, and $n = 51$ for both LED conditions) and burst spikes (red, Control versus LED $p = 3e-13$, control versus Double LED $p = 1e-15$, unpaired t test). (Right) Increase in burst ratio from the Control to LED condition, where burst ratio is defined as the number of burst spikes divided by the total number of spikes (Control versus LED $p = 9e-13$, control versus Double LED $p = 1.8e-11$, unpaired Wilcoxon rank-sum test).

(E) (Left) Example bursts for the Control and LED conditions. (Right) Increase in the mean number of spikes per burst from the Control to the LED condition (Control versus LED $p = 2.3e-5$, control versus Double LED $p = 1.7e-6$, unpaired Wilcoxon rank-sum test, $n = 54$ for control and $n = 51$ for each of the LED conditions). Error bars represent mean \pm SEM.

(F) Simulated spontaneous activity from integrate-and-fire-or-burst (IFB) model with hyperpolarizing input at time $t = 0$, showing all spikes (black) and burst spikes (red).

See STAR Methods and Figure S3.

we first probed the effect thalamic hyperpolarization has on baseline, ongoing activity that is significantly higher in the awake state compared with under anesthesia. An example single-unit (SU) VPm recording from the awake mouse (experimental setup

in Figure 2A) is shown in the raster plot in Figure 2B. VPm neurons in awake mice exhibited moderate ongoing firing, whereas the onset of the LED ramp caused an initial decrease in rate (population average, Figure 2C), followed by a brief increase above

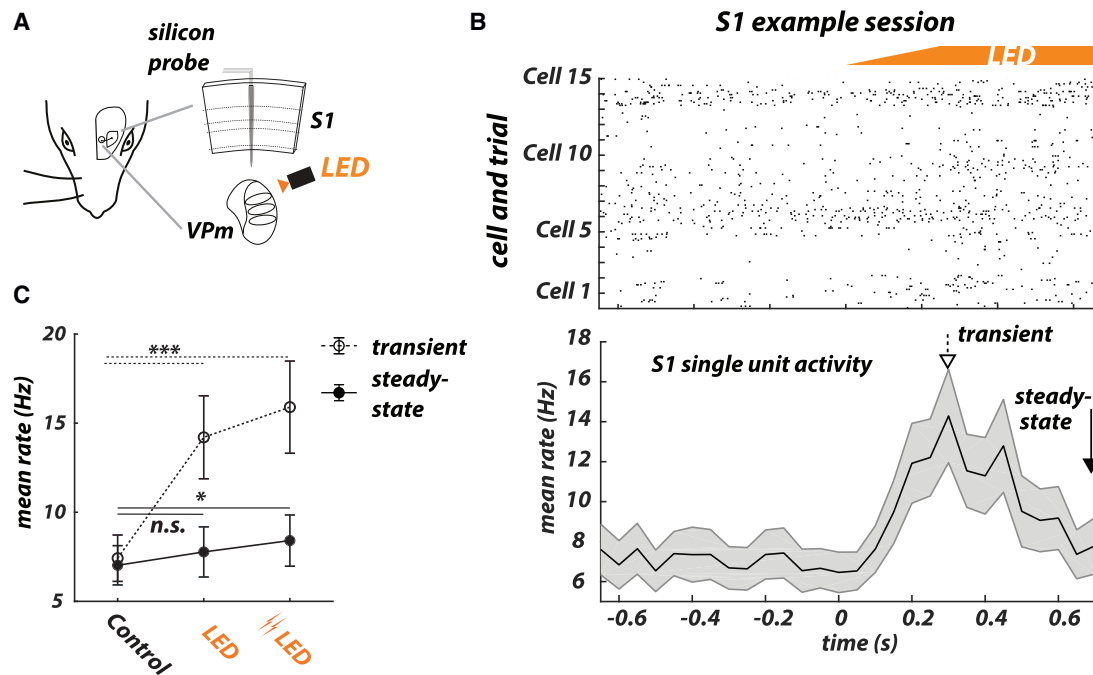


Figure 3. Cortical S1 baseline firing rate is invariant to optogenetic hyperpolarization of thalamus after transient increase

(A) Experimental setup. Mice were injected with the viral vector eNphR3.0 (AAV5-CamIIKiasse-eNphR3.0-mCherry) targeting the ventral posterior-medial (VPM) region of the thalamus. Thalamic units were continuously presented with light (590 nm, LED approx. 17 mW/mm² ramp, Double LED approx. 35 mW/mm² ramp) from a 200- μ m optic fiber, whereas cortical single units were recorded simultaneously with a laminar multi-electrode within an identified cortical column (barrel)—see STAR Methods.

(B) (Top) Example extracellular rasters of cortical activity, depicting effects of thalamic hyperpolarization on cortical spiking, across trials and simultaneously recorded units (10 trials each from 15 units). (Bottom) Aggregate PSTH across all recorded trials and cortical single units ($n = 118$). Bands represent mean \pm SEM. Highlighted are the transient and steady-state portions of the cortical response to the light.

(C) Mean cortical firing rate in the Control and LED conditions, showing an increase in the transient (open symbol, 300–350 ms, Control versus LED $p = 5.4e-14$, control versus Double LED $p = 1.4e-15$, Wilcoxon signed-rank test) and a return to near steady state (closed symbol, 700–750 ms, Control versus LED $p = 0.2$, control versus Double LED $p = 0.013$, Wilcoxon signed-rank test) portions of the response. Error bars represent mean \pm SEM.

pre-stimulus baseline firing rate, before returning to a level near baseline in the steady-state period. This effect is summarized by the mean firing rate over the entire period following the ramp (250–750 ms after LED onset, Figure 2D left), where there was no change in firing rate at the lowest light level and only a modest increase for the highest, likely influenced by the early transient increase. Restricting the mean to the steady-state phase of this response (700–750 ms after LED onset) revealed no change from the control condition (not shown). There was a corresponding significant increase in burst firing (red, Control versus LED), and in the ratio of burst to tonic spikes (Figure 2D, right). Increasing hyperpolarization also increased the number of spikes per burst (illustrated in left of Figure 2E), which partially offset the loss of tonic spiking (right of Figure 2E).

Although it is not surprising that the thalamic burst mechanism was engaged by the optogenetic hyperpolarization, it is surprising that the net baseline firing rate was not decreased but was instead approximately invariant to the thalamic hyperpolarization. This effect was not as apparent in the anesthetized condition when the baseline thalamic firing rate is near zero but emerges in the awake state where baseline thalamic firing rate is significantly higher. To further investigate, we constructed an integrate-and-fire-or-burst (IFB) model of thalamic firing that

has been utilized in previous studies (Smith et al., 2000; Lesica and Stanley, 2004; Lesica et al., 2006). In the model, the effect of the hyperpolarizing opsin activation indeed replicated this phenomenon (Figure 2F). An initial decrease in firing rate at the onset of the light ramp was followed by a transient increase and a return to pre-light baseline level of firing (compare with Figure 2C). Moreover, as in the experimental observation, the return to the baseline firing rate in the hyperpolarized condition is dominated by the increase in bursting activity in the IFB model (Figure 2F, red). The exact combination of the baseline activity and intensity of the hyperpolarizing input strongly influenced the net resultant effect (see Figure S3 for a range of baseline activity).

To uncover the downstream effects of the above observations in VPM, we performed the same manipulations during multi-electrode recording of SU activity in S1 in the awake mouse (Figure 3A). Note that for this analysis, these S1 recordings were combined across cortical layer and cell type, but subsequent analyses demonstrate similar trends across cell types and for targeted layer 4 recordings (see Figures 6 and S5). With thalamic hyperpolarization, mean rates increased dramatically during a transient (300–350 ms post-LED-onset) window but were only modestly elevated above baseline at steady state (700–750 ms post-onset).

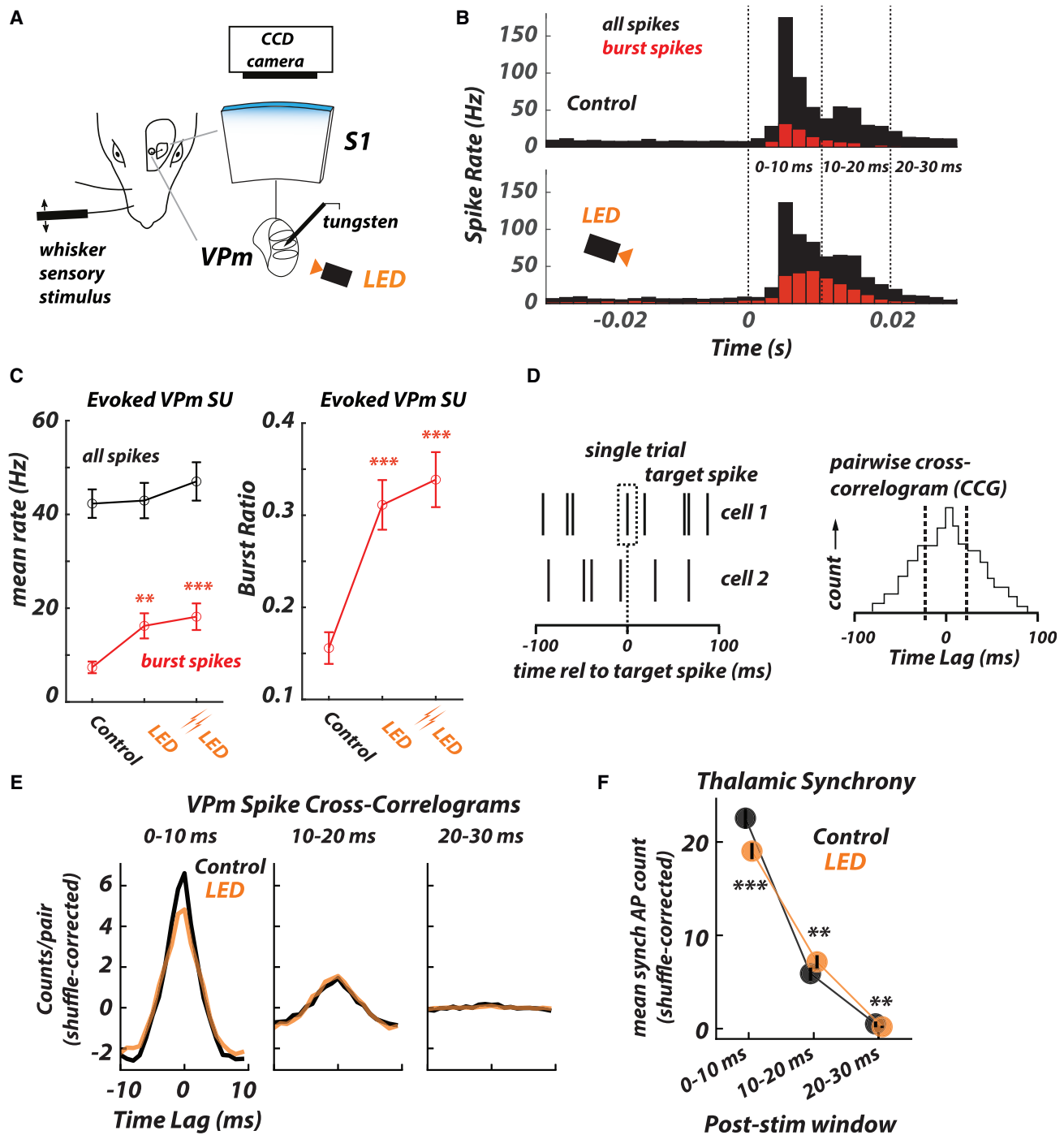


Figure 4. Thalamic hyperpolarization enhances the thalamic sensory-evoked bursting response in the awake mouse

(A) Experimental setup. Mice were injected with the viral vector eNphR3.0 (AAV5-CamIIKianse-eNphR3.0-mCherry) targeting the ventral posterior-medial (VPm) region of the thalamus and the viral vector ArcLight (AAV1-hyns1-ArcLightD-SV40) in the vibrissa region of the primary somatosensory cortex (S1). For optogenetic hyperpolarization, on each trial, thalamic units were presented with light for 1.5 s (590 nm, LED approx. 17 mW/mm² ramp, Double LED approx. 35 mW/mm² ramp—see STAR Methods) from a 200- μ m optic fiber, with LED illumination beginning at 0.75 s preceding stimulus delivery, and continuing for 0.75 s after stimulus delivery while recording simultaneously with a single tungsten electrode. For cortical GEVI imaging, the entire cortical area was illuminated through the thinned skull at 465 nm with an LED and imaged with a CCD imaging setup (see STAR Methods).

(B) Grand single-unit PSTH for thalamic spiking in response to a single, punctate whisker stimulus ($t = 0$) for the control (no light, top panel, $n = 54$ units) and LED (bottom panel, $n = 51$ units) conditions. Instantaneous firing rates (bin size 2 ms) shown for all spikes (black) and putative burst spikes (red).

(legend continued on next page)

Taken together, the results here suggest that in response to the optogenetically induced thalamic hyperpolarization, the thalamic VPm neurons in the awake mouse exhibit a transient change in baseline firing rate, followed by a return to approximately pre-hyperpolarization level that is at least partially explained by a trade-off between tonic and burst firing, whereas the downstream activity in cortical S1 exhibits a transient increase in baseline firing rate, followed by an eventual return to approximately the original baseline rates.

Thalamic hyperpolarization and sensory-evoked thalamic and cortical activity

We next recorded the sensory-evoked SU activity in VPm thalamus in the presence and absence of thalamic hyperpolarization in the awake mouse (Figure 4A). Neurons in VPm thalamus of the awake mouse responded to punctate whisker stimulation with a brief, transient increase in SU activity, which was significantly reshaped by thalamic hyperpolarization (Figure 4B). Thalamic hyperpolarization significantly increased sensory-evoked bursting (Figure 4C, left), although the overall (tonic + burst) mean evoked rate was unchanged (Figure 4C, left). This reflected a significant increase in the SU burst ratio (Figure 4C, right). Taken together, SU VPm analyses reveal a boosting of the sensory-evoked thalamic bursting with thalamic hyperpolarization, yet a surprisingly invariant overall mean evoked rate. Note that upon more careful inspection of the VPm peri-stimulus time histograms (PSTHs), thalamic hyperpolarization results in a qualitative decrease in the sensory-evoked response in the first 10 ms and a subsequent increase in the sensory-evoked response at later times. This could indicate changes in synchronous thalamic firing over the course of the sensory response, which is a critical factor in determining the downstream cortical response. To explicitly quantify this, we analyzed synchronous spiking of simultaneously recorded VPm pairs (Figure 4D), restricting the spiking activity to three nonoverlapping windows following the whisker stimulus (Figure 4E; see partitions in Figure 4B). Qualitatively, we observe a decrease in the central peak of the spike cross-correlogram (CCG) for the earliest post-stimulus time window (0–10 ms, left) from the Control to the LED condition and very little change for the two other time windows (10–20-ms middle, 20–30-ms right). We quantified this observation by computing the area in the region around the center of the CCG (–5 to +5 ms lags), representing the amount of synchronous spiking across the pairs. Most notably, the LED induced a decrease in the synchronous firing for the earliest post-stimulus time window (0–10 ms), when synchronous spike rates were generally highest. Synchronous spike

rates also changed in the two later response windows, when synchronous rates were generally lower, with a slight increase for the (10–20 ms) window and a slight decrease for the (20–30 ms) window. Thus, the VPm data reveal a significant boosting of sensory-evoked burst firing with thalamic hyperpolarization, accompanied by an approximately invariant overall sensory-evoked response magnitude and a surprising decrease in the synchrony of the prominent early thalamic response.

To examine the downstream consequences of the observed changes in the sensory-evoked response in thalamus, we recorded cortical S1 activation with wide-field optical voltage imaging during optogenetic hyperpolarization of thalamus in the awake mouse (Figure 5A; see STAR Methods). Based on previous findings (Swadlow and Gusev, 2001), the results in the anesthetized mouse, and the significant boosting of sensory-evoked bursting in thalamus with thalamic hyperpolarization in the awake mouse, we expected to see a corresponding amplification of the cortical sensory-evoked response. Surprisingly, thalamic hyperpolarization resulted in a 20%–40% decrease in the (relative) S1 sensory response (Figures 5A and 5B). Note that the right panel of Figure 5B is the same data as in the left panel, with each dataset normalized to the control condition, to show a percent decrease in the peak fluorescence. In a separate set of experiments, we hyperpolarized thalamus while simultaneously recording the S1 cortical SU responses (Figure 5C). The mean (absolute) S1 response to a 1,200²/s stimulus was approximately invariant to thalamic hyperpolarization (Figures 5D and 5E, left). However, the mean baseline-subtracted responses did decrease with increasing LED intensities, consistent with the (relative) GEVI recordings (Figure 5B). Note that the recorded cortical activity here was aggregated across cell type and cortical layer, but subsequent analyses will address cell type and layer (see Figures 6 and S5). Importantly, similar trends were observed through analysis restricted to putative layer 4 thalamorecipient cortical neurons (Figures S5A and S5B).

Thalamic bursting and the spatiotemporal shaping of the sensory-evoked cortical response

The GEVI imaging of cortex enables further investigation of the spatiotemporal characteristics of the observed phenomenon. Figure 5F shows the imaging frame associated with the peak sensory-evoked fluorescence, for the control (top) and thalamic hyperpolarization (LED, bottom) conditions, with an overall attenuation of the cortical evoked response with thalamic hyperpolarization. We next asked whether the reduced spatial activation simply reflected a uniform loss of amplitude across space (i.e., the “iceberg effect,” Figure 5G, left) or alternatively whether

(C) (Left) Mean sensory-evoked thalamic response over 0–30 ms time window for single-unit VPm recordings, for all spikes (black, Control versus LED $p = 0.9$, control versus Double LED $p = 0.4$, unpaired two-sample t test, $n = 54$ for control, and $n = 51$ for both LED conditions) and for burst spikes (red, Control versus LED $p = 0.003$, control versus Double LED $p = 1.6e-4$, unpaired Wilcoxon rank-sum test, $n = 54$ for control, $n = 51$ for both LED conditions). Error bars represent mean \pm SEM. (Right) Mean single-unit sensory-evoked thalamic burst ratio over the 0–30 ms time window (Control versus LED $p = 1.3e-5$, control versus Double LED $p = 2.4e-6$, unpaired Wilcoxon rank-sum test, $n = 54$ for control, and $n = 51$ for both LED conditions).

(D) Construction of spike cross-correlogram (CCG) from pairwise VPm spiking.

(E) Grand mean CCGs of the sensory-evoked response for the Control and LED conditions, when restricting spiking data to the (0–10 ms), (10–20 ms), and (20–30 ms) post-stimulus time windows ($n = 187$ simultaneously recorded pairs from 46 VPm single units, across 6 recording sessions).

(F) Mean shuffle-corrected synchronous spike count for the (0–10 ms), (10–20 ms), and (20–30 ms) post-stimulus time windows. All reported values are mean synch AP count \pm 99.95% confidence interval, resampling relative spike times with replacement ([0–10 ms], Control to LED, $p < 0.001$; [10–20 ms], $p < 0.01$; [20–30 ms], $p < 0.01$).

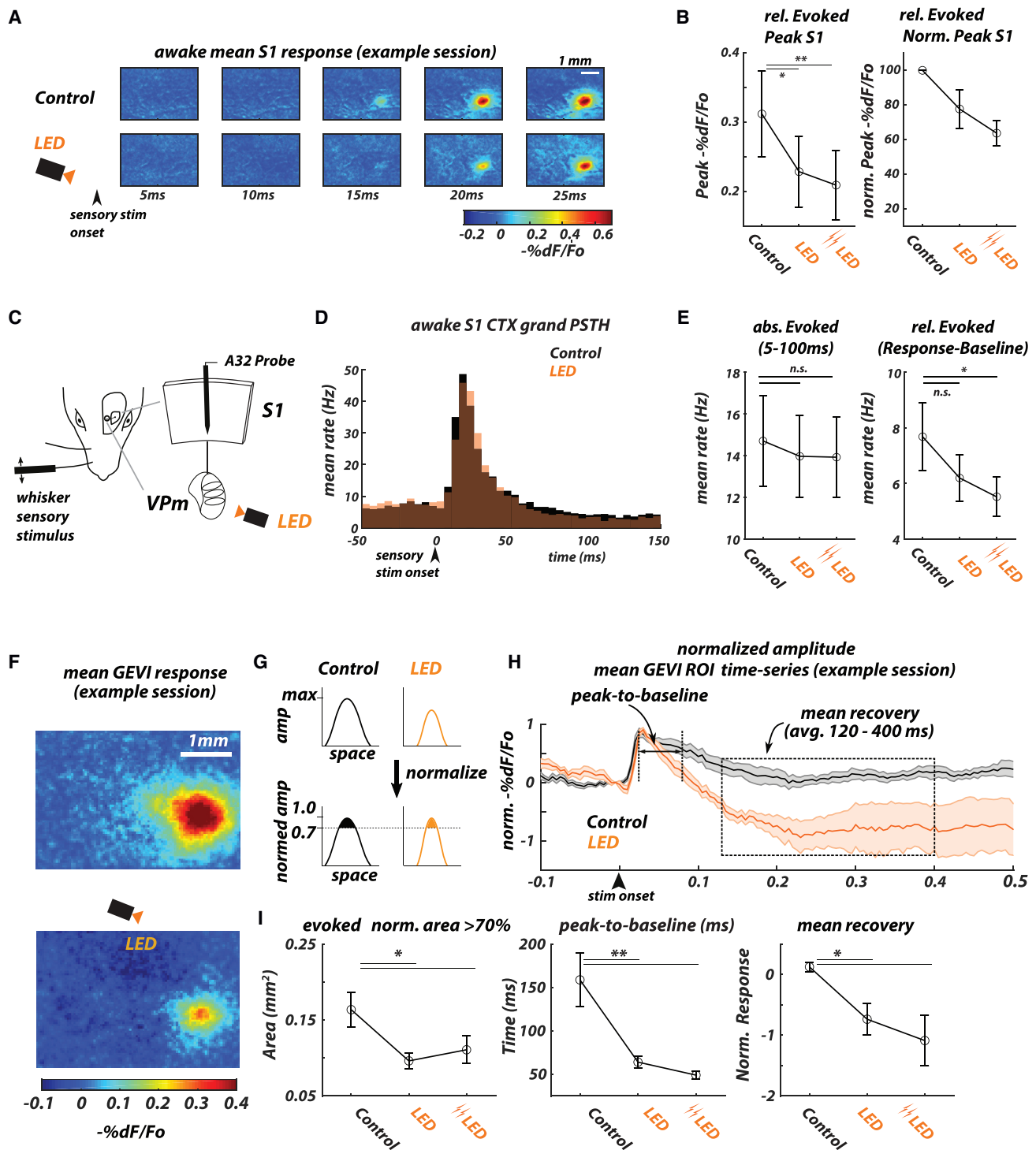


Figure 5. Cortical sensory-evoked response magnitude is invariant to thalamic hyperpolarization, but the cortical response is spatially sharpened and temporally narrowed

(A) Example session of GEVI imaging following the delivery of a punctate whisker stimulus at time $t = 0$, for the control (no light, top row) and LED (bottom row) conditions. Images are averaged across 51 trials.

(B) (Left) Peak GEVI sensory-evoked response (between 0 and 110 ms post-stimulus) slightly decreased from the control to the LED condition (Control versus LED $p = 0.020$, control versus Double LED $p = 0.0039$, paired Wilcoxon signed-rank test, $n = 9$ recordings from 2 mice). (Right) Mean normalized peak GEVI sensory-evoked response for the Control and LED conditions ($n = 9$ recordings). Before combining, animals and sessions were each normalized to their control levels, and the LED condition is reported relative to the control.

(legend continued on next page)

surrounding activation was disproportionately reduced relative to the central region, thus sharpening the representation (Figure 5G, right). We found the latter to be true: the evoked normalized area of activation was significantly reduced with thalamic hyperpolarization (Figure 5I, left).

In the fast temporal dynamics of the GEVI response (Figure 5H), the LED induced a more rapid, post-peak decay and a prolonged period of sub-baseline fluorescence before returning to baseline after several hundred milliseconds. Note that the fluorescence traces in Figure 5H are normalized to their peaks to focus on the temporal properties. We quantified the temporal width of the response as the “peak-to-baseline” (Figure 5H), which we found to decrease with increasing light levels (Figure 5I, center). We quantified the prolonged post-stimulus undershoot of activity as the “mean recovery” (Figure 5H), which became more pronounced with increasing light levels (Figure 5I, right). Thus, in addition to the attenuation of the sensory-evoked response with thalamic hyperpolarization, there is a corresponding sharpening of the spatial activation of S1 and a temporal narrowing/shortening in the form of a more transient-evoked response with an inhibitory undershoot.

Thalamic bursting and cortical spike timing

We further parsed our cortical SU into putative excitatory (RSUs, regular spiking units) and inhibitory (FSUs, fast-spiking units) neurons (Figure 6A; Guo et al., 2017; see STAR Methods). Note that although this analysis involved combining recordings across the electrode array, we conducted a parallel analysis restricted to a smaller population of identified cortical layer 4 RSUs and FSUs (see below, and Figure S5). Apparent in the aggregate PSTH is the expected higher baseline/ongoing activity and sensory-evoked responses in the FSUs compared with the RSUs (Figure 6B). Thalamic hyperpolarization induced a modest increase in baseline (−50–0 ms before sensory stimulus onset) rate for RSUs and an insignificant change for FSUs (Figure 6C, left). Further, hyperpolarization had little effect on the early (5–50 ms post-stimulus) S1 response; RSU rates increased modestly, and FSU rates did not change significantly (Figure 6C, center). Finally,

there was a qualitative change in shape of the PSTHs, with an increased latency to peak in the early phase and a noticeable dip below control rates in the late phase for both RSUs and FSUs (Figure 6B). This latter observation was reflected in a decrease in the late phase (60–100 ms) of the evoked response with increasing light levels (Figure 6C, right). In putative layer 4 thalamorecipient cortical cells, we observe very similar results to those shown for the larger aggregate dataset, and the trends we observed were qualitatively the same as shown in Figure 6 (see Figure S5).

The changes in timing and shape of the PSTHs of the cortical neurons suggest the possibility that thalamic hyperpolarization could affect synchronization within the cortical network. We further analyzed synchrony across simultaneously recorded cortical SU, calculated as the integrated area within a ± 7.5 ms window of the spike CCG (Figure 7A, bottom; see STAR Methods; Wang et al., 2010; Whitmire et al., 2016). Due to the sensitivity of the synchrony metric to firing rate, we only examined pairs with a robust measurement (more than 50 synchronous events) to control for measurement accuracy (experimental results were invariant with different thresholds, see STAR Methods), which restricted the analysis to FSUs in our dataset. Although thalamic hyperpolarization did not enhance the mean early evoked S1 rate (Figure 6), it did increase the rate of synchronous FSU spikes (Figure 7B). This resulted in an increased concentration of mass around 0 lag in the aggregate CCG (Figure 7C), and a significant increase in pairwise FSU synchrony with increasing light level (Figure 7D). For comparison, the synchrony was also computed for the ongoing, spontaneous activity, revealing the synchronizing effect of the transient sensory input. These results were qualitatively similar for various synchrony window sizes (not shown).

Modeling of the thalamic burst-driven cortical E-I circuit

We next sought to understand the mechanistic basis of two key experimental results: (1) the nearly invariant absolute S1 sensory response in the thalamic hyperpolarized (LED) condition in the awake mouse, despite the increase in sensory-evoked burst spikes in VPM and (2) the increase in sensory-evoked cortical synchrony in FS neurons in the thalamic hyperpolarized (LED)

(C) In separate experiments, we hyperpolarized the thalamus while simultaneously recording the S1 cortical response using a multichannel electrode.

(D) Cortical grand PSTH-evoked sensory response ($t = 0$) across all recorded single units ($n = 118$ units, 5 ms bins) for control (black) and LED (orange) conditions.

(E) (Left) Average absolute evoked cortical response remained approximately invariant during LED on conditions across all cortical recorded units ($n = 118$). Evoked sensory response period defined as between 5 and 100 ms post-stimulus. (Right) Relative-evoked cortical response decreased with increasing LED intensities (Control versus LED $p = 0.20$, control versus Double LED $p = 0.034$, paired Wilcoxon signed-rank test, $n = 118$ units). Relative-evoked response defined as the absolute response minus the preceding baseline activity −50–0 ms pre-stimulus. Error bars represent mean \pm SEM.

(F) GEVI imaging frames at peak response for the control (top) and LED (bottom) conditions for an example session.

(G) Cartoon illustration of the coupling between amplitude and spatial area in cortical imaging. (Top) A reduction in evoked fluorescence amplitude can be qualitatively perceived as a reduction in spatial area of activation, due to the “iceberg” effect. (Bottom) However, the spatial area of activation above a fixed threshold after normalization to the peak reveals the true effects on the area.

(H) Normalized amplitude time series of fluorescence within ROI for control (black) and thalamic hyperpolarized (orange, LED), $n = 9$ recordings from 2 mice conditions. Bands represent mean \pm SEM.

(I) Summary analyses (error bars represent mean \pm SEM). (Left) Mean spatial activation area of the normalized sensory-evoked response decreased from the Control to the LED condition (Control versus LED $p = 0.025$, control versus Double LED $p = 0.046$, paired t test, $n = 9$ recordings). (Middle) The peak-to-baseline (defined in H), calculated as the mean time from the peak of the fluorescence to the first return to pre-stimulus baseline (ms), decreased from the Control to the LED condition (Control versus LED $p = 0.0059$, control versus Double LED $p = 0.0019$, unpaired t test, $n = 8$ control recordings, 9 LED recordings, note one of the control recordings did not return to baseline). (Right) The recovery (defined in H), calculated as the relative mean fluorescence during the time duration following the peak stimulus-evoked response (120–400 ms), decreased from the Control to the LED condition (Control versus LED $p = 0.016$, control versus Double LED $p = 0.020$, paired t test, $n = 9$ recordings). LED approx. 17 mW/mm² ramp, Double LED approx. 35 mW/mm² ramp—see STAR Methods. Error bars represent mean \pm SEM.

See also Figure S4.

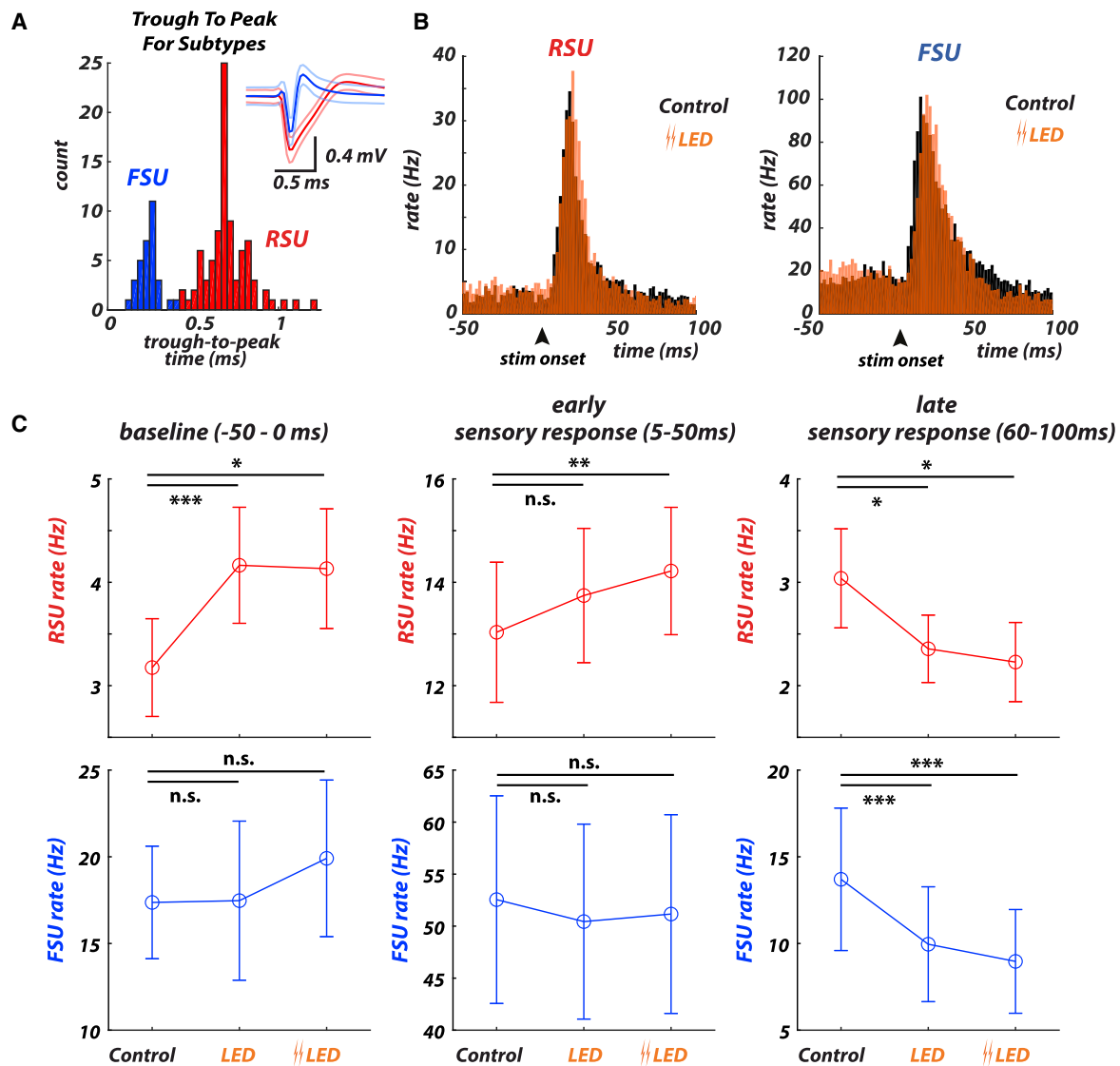


Figure 6. Thalamic hyperpolarization affects timing but not magnitude of sensory-evoked responses in cortex

(A) Cortical single units were classified as regular spiking units (RSUs, red) or fast-spiking units (FSUs, blue) based on the time interval from the peak-to-trough (see STAR Methods). Example RSU and FSU waveforms are shown at the top, where bands represent ± 1 SD. The distribution of time intervals from peak-to-trough for the spike waveforms is shown at the bottom.

(B) PSTHs of the aggregate putative RSUs (left, n = 86) and FSUs (right, n = 32) in response to a punctate whisker deflection at time t = 0 (bin size 2 ms) for the control (black) and double LED (orange) conditions.

(C) Summary analyses (error bars represent mean \pm SEM) for RSUs (top row) and FSUs (bottom row). (Left) Mean baseline (-50–0 ms) RSU (Control versus LED p = $5.3e-4$, control versus Double LED p = 0.012, Wilcoxon signed-rank test, n = 86) and FSU (Control versus LED p = 0.15, control versus Double LED p = 0.30, Wilcoxon signed-rank test, n = 32) firing rates for the LED relative to the control condition. (Middle) RSU (Control versus LED p = 0.067, control versus Double LED p = 0.0082, Wilcoxon signed-rank test, n = 86) and FSU (Control versus LED, p = 0.30, control versus Double LED p = 0.45, Wilcoxon signed-rank test, n = 32) early sensory response (5–50 ms) for the LED compared with the control conditions. (Right) Late sensory response (60–100 ms) for the LED compared with the control condition for the RSU (Control versus LED p = 0.017, control versus Double LED p = 0.014, n = 86, Wilcoxon signed-rank test) and FSU (Control versus LED p = $2.2e-4$, control versus Double LED p = $4.5e-4$, n = 32, Wilcoxon signed-rank test) populations. LED approx. 17 mW/mm² ramp, Double LED approx. 35 mW/mm² ramp—see STAR Methods. Error bars represent mean \pm SEM.

See also Figures S4 and S5.

condition. To explore the potential role of various thalamic and cortical mechanisms, we constructed a model of the TC network, as described previously (Wright et al., 2021). Briefly, the model consisted of an interconnected “L4” network of excit-

atory and inhibitory leaky integrate-and-fire neurons driven by empirically motivated tonic and burst “thalamic” spike trains (Figure 8A; see STAR Methods). For these input spike trains, the rate of synchronous spikes across conditions qualitatively

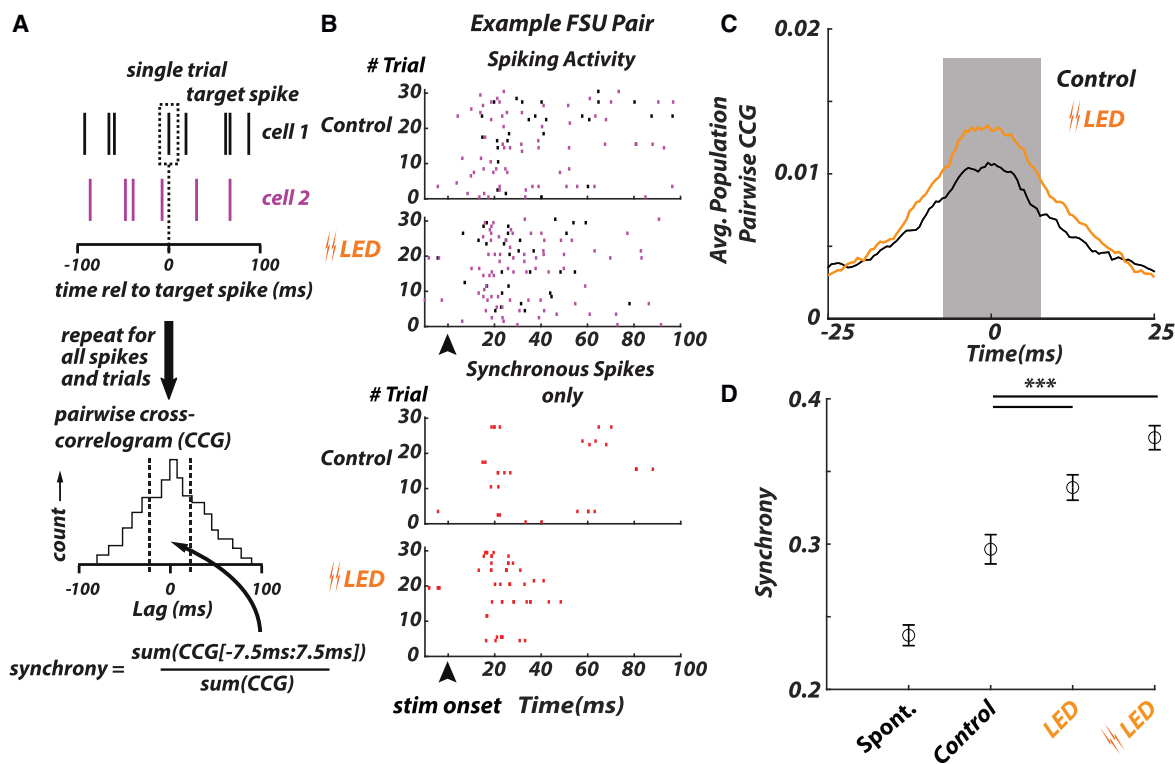


Figure 7. Thalamic hyperpolarization enhances cortical synchrony

(A) The spike cross-correlogram (CCG) was calculated as a histogram of spike times of cell 2 relative to a target spike of cell 1, repeated for all spikes of cell 1. The pairwise synchrony was calculated from the CCG as the area of the CCG between ± 7.5 ms, normalized by the total area of the CCG.

(B) (Top) Example raster of two simultaneously collected FSU units, Cell 1 (black), and Cell 2 (purple) for Control and LED conditions. (Bottom) Synchronous spiking events only for the same neural pair (red, firing within 7.5 ms of each other).

(C) Aggregate cross-correlograms for FSUs ($n = 99$ pairs, see STAR Methods) for the control (black) and LED (orange) conditions. Note that for the LED condition, the light level was 35 mW/mm^2 to better emphasize the change in synchrony with thalamic hyperpolarization. Cross-correlograms have been smoothed via a moving average filter, 2.5-ms window.

(D) Mean levels of synchrony for FSU pairs, for the spontaneous/baseline cortical firing compared with the sensory-evoked response for the control and LED conditions. Relative to the control condition, thalamic hyperpolarization (LED, 35 mW/mm^2) resulted in an increase in synchrony for the FSU populations (Control versus LED, $p = 1.5\text{e}-8$, control versus Double LED, $p = 3.5\text{e}-13$, Wilcoxon signed-rank test, $n = 99$ pairs). LED approx. 17 mW/mm^2 ramp, Double LED approx. 35 mW/mm^2 ramp—see STAR Methods. Error bars represent mean \pm SEM. See also Figure S4.

matched our experimental observations, with a slight but significant decrease in synchronous spiking in the short-latency response window from Control to LED (Figure 8B). For a more detailed description of the model, see STAR Methods.

This model network succeeded in qualitatively reproducing the two results identified above. First, despite the substantial increase in burst spikes in the thalamic inputs from the Control to LED condition (Figure 8A, top two rows), the network response amplitude was nearly invariant, with only a very slight increase (Figures 8A, bottom two rows and 8C). Second, we found that the evoked pairwise synchrony of S1 neurons was higher in the LED condition for both excitatory and inhibitory model neurons (Figure 8D). (Note that unlike the experimental data, synchrony measures from simulated cortical activity were not limited by lack of firing events, enabling synchrony measurements across both excitatory and inhibitory sub-populations.) In short, the mechanisms incorporated in this simple model were sufficient to predict the two key experimental results.

Having reproduced these results, we next sought to test the hypothesis that the nearly invariant mean cortical response despite the boosting of thalamic bursting represented the net effect of two opposing mechanisms: enhanced thalamic bursting in the LED condition supporting more robust TC synaptic drive, counterbalanced by a reduction in the rate of spikes that are synchronous across thalamic neurons. To this end, we manipulated the rate of synchronous thalamic input spikes while maintaining the mean rate of tonic and burst spikes, analogous to our previous work (Wang et al., 2010; Wright et al., 2021). Specifically, an artificial “randomized” condition was simulated in which tonic spike times were probabilistically shifted away from the early PSTH peak, such that the peak firing rate of this manipulated condition approximately matched that of the LED condition (Figure 8E, top). The grand VPM input CCG confirmed that this manipulation reduced the rate of synchronous input spikes (Figure 8F). The rate of tonic spikes in the 30-ms post-stimulus window was not altered and the burst spike distribution matched

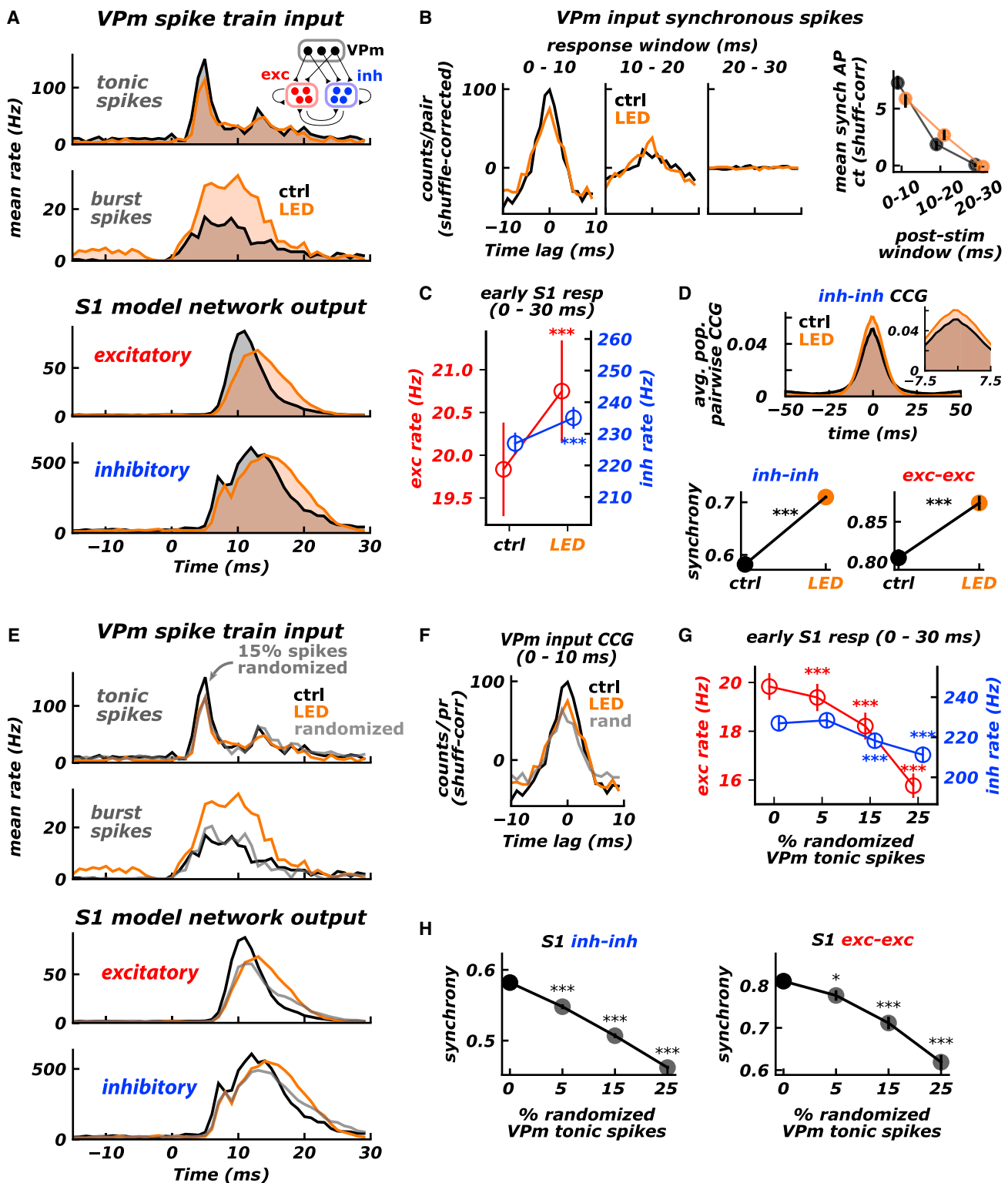


Figure 8. A thalamocortical network model reproduces key experiment results implicating thalamic spike timing

(A) Thalamocortical model schematic (see STAR Methods). (Top inset) A clustered network of excitatory (red) and inhibitory (blue) neurons received inputs from a model VPM barrelloid, as well as random excitatory inputs. (Top) Grand mean PSTHs for VPM tonic and burst spikes. (Bottom) Grand mean PSTHs for network excitatory and inhibitory neurons, for the control (black) and LED (orange) conditions.

(legend continued on next page)

the control condition, thus enabling the effects of such changes in synchronous spiking alone to be inferred. In contrast to the LED condition, shifting even small percentages of tonic VPM spikes (i.e., reducing the rate of synchronous VPM spikes) resulted in a significant decrease in cortical network response rates (Figure 8G) and synchrony (Figure 8H), with both measures decreasing monotonically with increasing percentage of shifted VPM spikes. These simulations thus support the notion that although thalamic bursting per se likely provides highly efficacious synaptic drive to cortex, the loss of short-latency, synchronous tonic firing in the LED condition counterbalances this effect, resulting in a nearly invariant S1 response. Further, the trends observed in cortical synchrony (Figure 8H) suggest thalamic bursts play an important role in synchronizing cortical neurons.

DISCUSSION

The sensory thalamus controls the flow of signaling from the periphery to cortex, ultimately gating what we do and do not perceive about the outside world. Despite its critical role in sensing, how this circuit controls signaling remains poorly understood. Here, through a range of experimental approaches in the awake, head-fixed mouse, we show that optogenetic thalamic hyperpolarization significantly enhances sensory-evoked bursting; however, the baseline thalamic firing rate and sensory-evoked magnitude are both approximately invariant. Sensory cortex subsequently exhibits a surprisingly invariant absolute evoked response despite the potent thalamic burst input, instead demonstrating increased timing precision, a focusing of spatial activation, and increased synchrony of spiking. TC network modeling further supports the assertion that the bursting-induced changes in thalamic spike timing and thalamic population synchrony are sufficient to explain the increase in cortical synchronization and the invariant cortical response amplitude, respectively. The findings here present a highly sensitive, timing-based gating of sensory signaling to cortex.

Thalamocortical gating of sensory signals

One surprising observation was that the absolute cortical sensory-evoked response amplitude was invariant to thalamic hyperpolarization in awake mice, despite a significant increase in

thalamic bursting. At first glance, this appears to contradict previous work clearly demonstrating the increased efficacy with which bursts in individual thalamic neurons impact monosynaptically-connected cortical neurons at the single synapse level (Swadlow and Gusev, 2001). Importantly, however, the efficacy with which a population of thalamic neurons drives cortical spiking depends on relative spike timing both within a given thalamic neuron (i.e., tonic versus burst) and across convergent thalamic neurons (i.e., degree of synchronization). We found that although thalamic hyperpolarization promoted single-neuron bursting, there was a surprising decrease in synchronous thalamic firing in the critical early sensory-evoked response. The nearly invariant cortical response makes sense in light of this observation; cortex is extremely sensitive to thalamic spike timing over this 10-ms period established by the disynaptic inhibition mediated “window of opportunity” (Pinto et al., 2000; Wilent and Contreras, 2004, 2005; Gabernet et al., 2005). The findings here thus coexist with the potency of thalamic bursts in driving post-synaptic cortical responses at the single synapse level.

Although the absolute cortical response amplitude was nearly invariant to thalamic hyperpolarization, the timing precision and synchrony of the cortical response were enhanced by our manipulation. Such changes in cortical representations suggest a more potent input for subsequent downstream signaling and perhaps enhanced stimulus detectability—despite the invariance of S1 firing rate—but corresponding recordings of the S1 recipient regions and a behavioral assay would be needed to test this hypothesis directly. We also note that the observed changes in FS synchrony likely play a role in shaping the overall cortical response we observe, as well as shaping the cortical sensitivity to timing of the thalamic input through direct interactions with the excitatory cortical sub-population, but a full exploration of the excitatory/inhibitory interactions within cortex was beyond the scope of this investigation. Further, the nature of the short inter-spike intervals (ISIs) within thalamic bursts almost certainly means that depression at the TC synapse plays a role in determining the potency of the sensory-evoked cortical response, as has been previously shown. However, the modeling results here suggest that single-neuron bursting and across-neuron synchronous thalamic firing, and how they interact with the timing sensitivity of cortex established by the disynaptic

(B) (Left) Grand spike cross-correlograms for VPM spike train inputs to the model cortical network, for three post-stimulus windows. (Right) Mean synchronous spike counts for VPM spike train inputs to the model cortical network. Error bars indicate 95% confidence intervals from resampling relative spike times with replacement.

(C) Grand mean (\pm SEM) rates for all model network excitatory (red) and inhibitory (blue) neurons for the early (0–30 ms post-stim) response window. Excitatory control versus LED: 4.6% increase, $p = 6.85 \times 10^{-9}$, Wilcoxon signed-rank test. Inhibitory control versus LED: 3.6% increase, $p = 2.15 \times 10^{-13}$, Wilcoxon signed-rank test.

(D) (Top) Grand cross-correlograms for 200 randomly selected, valid pairs of network inhibitory neurons (see STAR Methods). (Inset) Same, but for window used to calculate synchrony (± 7.5 ms). (Bottom) Grand mean (\pm SEM) pairwise synchrony for 200 valid inhibitory pairs (left) and 147 valid excitatory pairs (right). Inh-inh control versus LED: 22.4% increase, $p = 1.44 \times 10^{-34}$, Wilcoxon signed-rank test. Exc-exc control versus LED: 8.4% increase, $p = 1.74 \times 10^{-7}$, Wilcoxon signed-rank test.

(E) Same as in (A), but including “randomized” condition (gray PSTHs), in which $p = 15\%$ of drawn tonic spike times occurring near the early PSTH peak were shifted to a later, random time.

(F) Same as in (B, left), but including “randomized” condition (gray CCG).

(G) Same as in (C), but for various choices of p (percent randomized VPM tonic spike times).

(H) Same as in (D, bottom), but for various choices of p . * indicates $0.01 \leq p < 0.05$, ** indicates $0.001 \leq p < 0.01$, *** indicates $p < 0.001$, Wilcoxon signed-rank test.

feedforward inhibition, are the key role players in the observed dynamics, although more extensive experiments involving causal manipulations of these mechanisms would need to be conducted to more conclusively establish this explanation. Finally, although not explicitly tested in these experiments, the results here would suggest that important coding aspects of this particular pathway, notably velocity and direction tuning, would be strongly shaped through changes in the timing properties of the thalamic population, as we have previously shown in the context of rapid sensory adaptation (Wang et al., 2010).

In several of the analyses here, we combined recorded cortical units across layers. Although the optical GEVI imaging approach is focused on S1 layer 2/3, it also likely captures activity above and below layer 2/3, as well as any cross-laminar processes, and further obscures any differences across excitatory and inhibitory sub-populations due to the indiscriminate viral targeting. Neurons in VPm thalamus send axonal projections differentially across laminae in S1 (Sermet et al., 2019), likely resulting in variations in the effects of thalamic hyperpolarization on S1 neurons in different cortical layers. To account for the possibility that the pooled dataset was not representative of thalamorecipient neurons, we repeated a subset of our analyses for putative S1 layer 4 neurons, and in each case, we observed the same trends as in the aggregate data (Figure S5). Note that the identification of L4 neurons was conducted conservatively, and thus, some of the non-L4 neurons in the aggregate population are likely also L4. Importantly, the putative L4 neurons had a larger sensory-evoked response than the non-L4 neurons, as is apparent in comparing Figure S5 with Figures 5 and 7, thus likely dominating the aggregate analysis. Further, note that although the measurements of synchrony in S1 here were limited to the putative FS neurons due to the relatively low firing rates of the RS neurons, the modeling results suggest that the RS neurons would also exhibit an increase in synchrony with thalamic hyperpolarization, but this must be directly measured in future studies. Regardless, the qualitative consistency of our cortical results across cell types, laminar location, and recording modalities suggest that our observations provide a representative—although by no means comprehensive—view of the net effects of thalamic spike timing on cortical sensory responses.

Invariance in baseline thalamic firing activity

In this study, we utilized optogenetic hyperpolarization to bias thalamic sensory responses toward bursting, without significantly changing other dynamics that might indirectly impact sensory responses. One particularly surprising finding here was that despite optogenetically induced hyperpolarization of thalamus, the overall baseline firing rate of thalamic neurons was not suppressed, but instead unchanged. Following a transient decrease in firing rate and then an increase above baseline, the recorded VPm neurons returned to their original baseline firing rate. This finding is, however, consistent with other reported observations. In the visual pathway, for example, optogenetic excitation of the thalamic-reticular nucleus (TRN) transiently silences the lateral geniculate nucleus, followed by a return to the original firing rate at steady state (Reinhold et al., 2015). In the somatosensory pathway, strong photoinhibition attenuated VPm thalamic firing rate but failed to quench activity altogether (Halassa et al.,

2011; Poulet et al., 2012; Lewis et al., 2015; Reinhold et al., 2015; Yu et al., 2016). The most parsimonious explanation given the observations here is that moderate amounts of hyperpolarization serve to engage the dynamics of the T-type calcium channels that are inactive at normal baseline conditions, effectively compensating for the loss in tonic spiking due to the hyperpolarization. Although the optogenetic approach here does not enable direct observation of the magnitude of the hyperpolarizing input, separate intracellular *in-vitro* slice experiments where we repeated the protocol while patching on to VPm neurons revealed relatively modest amounts of hyperpolarization that were well sustained during constant light illumination. This is important, as recent studies have suggested that prolonged activation of specific opsins can have unintended consequences, notably here, the possibility of changes in the reversal potential for chloride (Raimondo et al., 2012). This effect could theoretically result in changes in the degree of hyperpolarization, although halorhodopsin as a pump is less directly affected by immediate (local) changes in reversal potential compared with channel-based optogenetics. Further, with halorhodopsin, there is the potential for photoinactivation and decreased photocurrents (Zhang et al., 2019), which could also change the degree of hyperpolarization over time. Through the combination of the intracellular control experiments and replication of the primary result through the IFB model, the likelihood that these possible effects played a primary role here is low, especially over the relatively short time-scales considered here.

Importantly, beyond the engagement of the T-type calcium channel burst mechanism upon initial hyperpolarization, it would seem that additional hyperpolarization would further push the neuron away from threshold, making it more difficult to burst, which would predict a corresponding decrease in firing rate. However, we found that increased hyperpolarization increased the number of spikes per burst, which served to offset the decrease in the number of bursts with increasing hyperpolarization. The result is a surprisingly resilient mechanism in response to this perturbation. It should be noted that other elements of the circuit likely play a role in the observation here—for example, the initial decrease in VPm firing rate would decrease excitation of TRN, subsequently decreasing inhibition of VPm, which would work synergistically with the intrinsic properties of the burst mechanism in this compensatory action.

The potential role of thalamic bursts in sensory signaling

Almost four decades ago, Crick proposed a provocative hypothesis—that the thalamic-reticular complex serves as a dynamic gate for attentional control of sensory signaling to cortex (Crick, 1984). Further refinement of this idea suggested that the switching between tonic and burst firing modes of thalamic neurons that is facilitated by the unique dynamics of the T-type calcium channels that are prevalent in the thalamus could establish a context dependent signaling (Sherman and Guillery, 2002; Sherman, 2005). In this framework, burst spiking would promote the detection of salient sensory features, whereas tonic spiking would promote the transmission of details about the nature of the sensory stimulus. Furthermore, the thalamic burst would also potentially provide a “wake-up call” to cortex (Sherman, 2001a), garnering attentional resources that ultimately would

serve to switch the thalamic mode of firing to tonic through depolarizing corticothalamic feedback. As attractive a framework as this is, it is also a daunting theory to test experimentally due to the complexity of the circuit, the required specificity of recording and manipulation, and, ultimately, the need to cast in the context of changing states of arousal during trained behaviors. Previous anesthetized studies have made substantial progress toward this goal. For example, sensory-evoked thalamic bursting under anesthesia has been shown to be well driven by the appearance of salient sensory features (Lesica and Stanley, 2004; Alitto et al., 2005; Denning and Reinagel, 2005), which promotes the detection of change in the sensory input from the perspective of an ideal observer of thalamic spiking (Lesica and Stanley, 2004), and this sensitivity is strongly shaped by thalamic state (Lesica et al., 2006). Further studies showing the sensitivity of sensory cortex to spontaneous (non-sensory) thalamic bursting during wakefulness (Swadlow and Gusev, 2001) seem to set the stage for at least part of the overarching coding scheme in which the cortical response would be amplified by the thalamic bursts in “detect” mode.

In opposition to this view, some have noted that because ongoing thalamic spontaneous bursting events are particularly prominent during slow wave sleep and under anesthesia, they likely play no role in sensory signaling during wakefulness. However, this has been largely disproven, with low rates of bursts occurring both spontaneously and during naturalistic stimuli in awake somatosensory (Swadlow and Gusev, 2001; Stoelzel et al., 2009; Wright et al., 2021), visual (Niell and Stryker, 2010), and auditory systems (Massaux et al., 2004). Further, we have shown previously in the awake, head-fixed rat (Whitmire et al., 2016) and mouse (Wright et al., 2021) that rapid sensory adaptation has a particularly strong effect on sensory-evoked burst firing, suggesting that the adaptive changes in bursting may play an important role in perceptual adaptation during wakefulness. Thus, it is critical to precisely probe the effects of sensory-evoked thalamic bursting on cortical sensory representations during wakefulness and specifically to test the decades-old “wake-up call” hypothesis.

To this end, an optogenetic manipulation approach was adopted to gain systematic control over thalamic burst/tonic firing modes, and the functional effects were precisely quantified at the level of thalamus and primary sensory cortex. During normal physiological conditions, the thalamus receives a range of complex, excitatory and inhibitory inputs that interact with the intrinsic cell properties to collectively set the baseline membrane potential and firing rate of these neurons as a function of behavioral state. Cortex also exhibits profound changes in ongoing and sensory-evoked firing across states of wakefulness, and there is strong evidence that thalamic activity itself is a prominent driver of cortical state (Poulet et al., 2012). However, because thalamus and cortex are densely interconnected through feedforward and feedback projections and are both subject to a range of other modulatory inputs, it is generally difficult to infer directions of causality. The approach here enabled the disentangling of these interactions by probing the downstream effects of sensory-evoked thalamic bursting and synchronous firing per se, independent of the many other naturally occurring fluctuations. We do not suggest that the thalamic hyperpolarization mimics a particular behavioral state but rather that it provides an opportunity to bias thalamic

sensory responses toward burst firing mode, so that we might probe the consequences for cortex. Such targeted manipulations are critical to understanding state-dependent sensory signaling in this complex circuit more generally.

In the experiments presented here, in the absence of optogenetic manipulation, bursting represents approximately 15% of the total sensory-evoked response, compared with greater than 30% during imposed thalamic hyperpolarization. Thus, even in the absence of optogenetic manipulation, the bursting is not insignificant, and determining the effects of thalamic bursts on cortex is relevant even under normal conditions. It is also important to note that awake, head-fixed mice likely explore a much narrower range of behavioral (e.g., arousal) states than occur in naturalistic settings. It is well known that states of low arousal are directly correlated with thalamic burst firing modes, thus predictive of more sensory-evoked burst firing than we observed here. Although the experimental preparation used here provides the requisite stability to perform precise stimulation and recording, a complementary scenario for exploring the role of bursting across states of wakefulness would involve freely moving rodents visiting a wider range of behavioral states. These kinds of studies, in concert with those providing even more precise control of thalamic firing modes (e.g., via closed-loop feedback control of neural activity; Bolus et al., 2018, 2021) need to be employed to more effectively and comprehensively explore the coupling across brain regions and behavioral states.

Although the results here in the awake brain demonstrate that the absolute S1 sensory-evoked response was invariant to thalamic hyperpolarization and even diminished relative to background cortical activity despite potent sensory-evoked thalamic bursting, what emerges is increased timing precision, increased focus of spatial activation, and a corresponding synchronization of the cortical sensory-evoked response that collectively could promote detectability. Given the likely timing sensitivity of downstream brain structures in the sensorimotor arc, the synchronization of cortical activity may in fact be a more critical element of cortical signaling than overall magnitude, supported by behavioral work demonstrating the importance of cortical synchrony over firing rate (Jadhav et al., 2009). Taken together, the results here point to timing rather than response magnitude as a fundamental currency of the TC circuit, presenting a dynamic, timing-based gating of sensory signaling to cortex that has strong implications for detectability and discriminability in complex sensory environments.

STAR★METHODS

Detailed methods are provided in the online version of this paper and include the following:

- KEY RESOURCES TABLE
- RESOURCE AVAILABILITY
 - Lead contact
 - Materials availability
 - Data and code availability
- EXPERIMENTAL MODEL AND SUBJECT DETAILS
- METHOD DETAILS
 - AAV delivery

- Awake Animal Preparation
- Whisker stimulation
- Thalamic and cortical electrophysiology
- Awake cortical fluorescent arclight imaging
- Anesthetized cortical fluorescent arclight & intrinsic imaging
- Functional fluorescent mapping of barrel cortex
- Simultaneous imaging and thalamic optogenetic manipulation
- Anesthetized electrophysiology
- Histology
- Integrate & Fire or Burst (IFB) Modeling
- Cortical E-I modeling
- Model of VPM barreloid
- Thalamocortical connectivity
- Model of S1 network
- **QUANTIFICATION AND STATISTICAL ANALYSIS**
 - Thalamic electrophysiology data analysis - Mean response, burst ratio, synchronous spike counts
 - Thalamic and cortical electrophysiology data analysis
 - Voltage imaging data processing
 - Awake voltage imaging data analysis – Dual camera
 - Imaging data analysis – Peak amplitude, normalized peak, and temporal properties
 - Imaging data analysis – Area measurements
 - Statistical analysis

SUPPLEMENTAL INFORMATION

Supplemental information can be found online at <https://doi.org/10.1016/j.neuron.2022.06.008>.

ACKNOWLEDGMENTS

This work was supported by NIH National Institute of Neurological Disorders and Stroke grant R01-NS048285 (G.B.S.), R01-NS104928 (G.B.S.), U01-NS094302 (G.B.S. and D.J.), and NIH National Institute of Neurological Disorders and Stroke Pre-doctoral NRSA NS098691 (P.Y.B.). The authors would like to thank Katie Borden, Ilya Kolb, Will Stoy, and Precision Biosystems Lab at Georgia Tech, for additional support and advice on analysis. The authors also thank Elaida Dimwamwa and Aurélie Pala for assistance with cortical laminar assignment, and Aurélie Pala for assistance with spike-sorting.

AUTHOR CONTRIBUTIONS

P.Y.B., N.C.W., and G.B.S. conceptualized the study. P.Y.B. and N.C.W. conducted the investigation, including performing the experiments, curating the data, and conducting the formal analysis. P.Y.B., N.C.W., and G.B.S. wrote the original draft. D.J., B.H., and A.E.M. contributed to writing of the original draft and review/editing.

DECLARATION OF INTERESTS

The authors declare no competing interests.

Received: July 26, 2021
Revised: March 4, 2022
Accepted: June 7, 2022
Published: July 7, 2022

REFERENCES

- Aguilar, J.R., and Castro-Alamancos, M.A. (2005). Spatiotemporal gating of sensory inputs in thalamus during quiescent and activated states. *J. Neurosci.* *25*, 10990–11002.
- Alitto, H.J., Weyand, T.G., and Usrey, W.M. (2005). Distinct properties of stimulus-evoked bursts in the lateral geniculate nucleus. *J. Neurosci.* *25*, 514–523.
- Barthó, P., Slézia, A., Mátyás, F., Faradzs-Zade, L., Ulbert, I., Harris, K.D., and Acsády, L. (2014). Ongoing network state controls the length of sleep spindles via inhibitory activity. *Neuron* *82*, 1367–1379.
- Béhuret, S., Deleuze, C., and Bal, T. (2015). Corticothalamic synaptic noise as a mechanism for selective attention in thalamic neurons. *Front. Neural Circuits* *9*, 80.
- Bolus, M.F., Willats, A.A., Rozell, C.J., and Stanley, G.B. (2021). State-space optimal feedback control of optogenetically driven neural activity. *J. Neural Eng.* *18*, 036006.
- Bolus, M.F., Willats, A.A., Whitmire, C.J., Rozell, C.J., and Stanley, G.B. (2018). Design strategies for dynamic closed-loop optogenetic neurocontrol in vivo. *J. Neural Eng.* *15*, 026011.
- Borden, P.Y., Ortiz, A.D., Waiblinger, C., Sederberg, A.J., Morrisette, A.E., Forest, C.R., Jaeger, D., and Stanley, G.B. (2017). Genetically expressed voltage sensor ArcLight for imaging large scale cortical activity in the anesthetized and awake mouse. *Neurophotonics* *4*, 031212.
- Brecht, M., and Sakmann, B. (2002). Whisker maps of neuronal subclasses of the rat ventral posterior medial thalamus, identified by whole-cell voltage recording and morphological reconstruction. *J. Physiol.* *538*, 495–515.
- Bruno, R.M., and Sakmann, B. (2006). Cortex is driven by weak but synchronously active thalamocortical synapses. *Science* *312*, 1622–1627.
- Bruno, R.M., and Simons, D.J. (2002). Feedforward mechanisms of excitatory and inhibitory cortical receptive fields. *J. Neurosci.* *22*, 10966–10975.
- Crandall, S.R.R., Cruikshank, S.J.J., Connors, B.W.W., Crandall, S.R.R., Cruikshank, S.J.J., and Connors, B.W.W. (2015). A corticothalamic switch: controlling the thalamus with dynamic synapses. *Neuron* *86*, 1–15.
- Crick, F. (1984). Function of the thalamic reticular complex: the searchlight hypothesis. *Proc. Natl. Acad. Sci. USA* *81*, 4586–4590.
- Cruikshank, S.J., Lewis, T.J., and Connors, B.W. (2007). Synaptic basis for intense thalamocortical activation of feedforward inhibitory cells in neocortex. *Nat. Neurosci.* *10*, 462–468.
- Denning, K.S., and Reinagel, P. (2005). Visual control of burst priming in the anesthetized lateral geniculate nucleus. *J. Neurosci.* *25*, 3531–3538.
- Fogerson, P.M., and Huguenard, J.R. (2016). Tapping the brakes: cellular and synaptic mechanisms that regulate thalamic oscillations. *Neuron* *92*, 687–704.
- Gabernet, L., Jadhav, S.P., Feldman, D.E., Carandini, M., and Scanziani, M. (2005). Somatosensory integration controlled by dynamic thalamocortical feed-forward inhibition. *Neuron* *48*, 315–327.
- Gerfen, C.R., Paletzki, R., and Heintz, N. (2013). GENSAT BAC cre-recombinase driver lines to study the functional organization of cerebral cortical and basal ganglia circuits. *Neuron* *80*, 1368–1383.
- Godwin, D.W., Vaughan, J.W., and Sherman, S.M. (1996). Metabotropic glutamate receptors switch visual response mode of lateral geniculate nucleus cells from burst to tonic. *J. Neurophysiol.* *76*, 1800–1816.
- Gradinaru, V., Zhang, F., Ramakrishnan, C., Mattis, J., Prakash, R., Diester, I., Goshen, I., Thompson, K.R., and Deisseroth, K. (2010). Molecular and cellular approaches for diversifying and extending optogenetics. *Cell* *141*, 154–165.
- Guo, W., Clause, A.R., Barth-Maron, A., and Polley, D.B. (2017). A corticothalamic circuit for dynamic switching between feature detection and discrimination. *Neuron* *95*, 180–194.e5.
- Halassa, M.M., Siegle, J.H., Ritt, J.T., Ting, J.T., Feng, G., and Moore, C.I. (2011). Selective optical drive of thalamic reticular nucleus generates thalamic bursts and cortical spindles. *Nat. Neurosci.* *14*, 1118–1120.

- Hirata, A., and Castro-Alamancos, M.A. (2010). Neocortex network activation and deactivation states controlled by the thalamus. *J. Neurophysiol.* *103*, 1147–1157.
- Huguenard, J.R., and McCormick, D.A. (2007). Thalamic synchrony and dynamic regulation of global forebrain oscillations. *Trends Neurosci.* *30*, 350–356.
- Isaacson, J.S., and Scanziani, M. (2011). How inhibition shapes cortical activity. *Neuron* *72*, 231–243.
- Jadhav, S.P., Wolfe, J., and Feldman, D.E. (2009). Sparse temporal coding of elementary tactile features during active whisker sensation. *Nat. Neurosci.* *12*, 792–800.
- Jahnson, H., and Llinás, R. (1984a). Voltage-dependent burst-to-tonic switching of thalamic cell activity: an in vitro study. *Arch. Ital. Biol.* *122*, 73–82.
- Jahnson, H., and Llinás, R. (1984b). Electrophysiological properties of guinea-pig thalamic neurones: an in vitro study. *J. Physiol.* *349*, 205–226.
- Jin, L., Han, Z., Platasa, J., Wooltorton, J.R.A., Cohen, L.B., and Pieribone, V.A. (2012). Single action potentials and subthreshold electrical events imaged in neurons with a fluorescent protein voltage probe. *Neuron* *75*, 779–785.
- Kimura, F., Itami, C., Ikezoe, K., Tamura, H., Fujita, I., Yanagawa, Y., Obata, K., and Ohshima, M. (2010). Fast activation of feedforward inhibitory neurons from thalamic input and its relevance to the regulation of spike sequences in the barrel cortex. *J. Physiol.* *588*, 2769–2787.
- Kirchgessner, M.A., Franklin, A.D., and Callaway, E.M. (2020). Context-dependent and dynamic functional influence of corticothalamic pathways to first- and higher-order visual thalamus. *Proc. Natl. Acad. Sci. USA* *117*, 13066–13077.
- Lesica, N.A., and Stanley, G.B. (2004). Encoding of natural scene movies by tonic and burst spikes in the lateral geniculate nucleus. *J. Neurosci.* *24*, 10731–10740.
- Lesica, N.A., Weng, C., Jin, J., Yeh, C.-I., Alonso, J.-M., and Stanley, G.B. (2006). Dynamic encoding of natural luminance sequences by LGN bursts. *PLoS Biol.* *4*, e209.
- Lewis, L.D., Voigts, J., Flores, F.J., Schmitt, L.I., Wilson, M.A., Halassa, M.M., and Brown, E.N. (2015). Thalamic reticular nucleus induces fast and local modulation of arousal state. *eLife* *4*, e08760.
- Li, L., and Ebner, F.F. (2016). Cortex dynamically modulates responses of thalamic relay neurons through prolonged circuit-level disinhibition in rat thalamus in vivo. *J. Neurophysiol.* *116*, 2368–2382.
- Lu, S.M., Guido, W., and Sherman, S.M. (1992). Effects of membrane voltage on receptive field properties of lateral geniculate neurons in the cat: contributions of the low-threshold Ca²⁺ conductance. *J. Neurophysiol.* *68*, 2185–2198.
- Lustig, B.R., Friedman, R.M., Winberry, J.E., Ebner, F.F., and Roe, A.W. (2013). Voltage-sensitive dye imaging reveals shifting spatiotemporal spread of whisker-induced activity in rat barrel cortex. *J. Neurophysiol.* *109*, 2382–2392.
- Ma, Y., Shaik, M.A., Kim, S.H., Kozberg, M.G., Thibodeaux, D.N., Zhao, H.T., Yu, H., and Hillman, E.M.C. (2016). Wide-field optical mapping of neural activity and brain haemodynamics: considerations and novel approaches. *Philos. Trans. R. Soc. Lond. B Biol. Sci.* *371*, 20150360.
- Massaux, A., Dutrieux, G., Cotillon-Williams, N., Manunta, Y., and Edeline, J.M. (2004). Auditory thalamus bursts in anesthetized and non-anesthetized states: contribution to functional properties. *J. Neurophysiol.* *91*, 2117–2134.
- McCormick, D.A., Connors, B.W., Lighthall, J.W., and Prince, D.A. (1985). Comparative electrophysiology of pyramidal and sparsely spiny stellate neurons of the neocortex. *J. Neurophysiol.* *54*, 782–806.
- Mease, R.A., Krieger, P., and Groh, A. (2014). Cortical control of adaptation and sensory relay mode in the thalamus. *Proc. Natl. Acad. Sci. USA* *111*, 6798–6803.
- Millard, D.C., Whitmire, C.J., Gollnick, C.A., Rozell, C.J., and Stanley, G.B. (2015). Electrical and optical activation of mesoscale neural circuits with implications for coding. *J. Neurosci.* *35*, 15702–15715.
- Niell, C.M., and Stryker, M.P. (2010). Modulation of visual responses by behavioral state in mouse visual cortex. *Neuron* *65*, 472–479.
- Olsen, S.R., Bortone, D.S., Adesnik, H., and Scanziani, M. (2012). Gain control by layer six in cortical circuits of vision. *Nature* *483*, 47–52.
- Owen, S.F., Liu, M.H., and Kreitzer, A.C. (2019). Thermal constraints on in vivo optogenetic manipulations. *Nat. Neurosci.* *22*, 1061–1065.
- Pinto, D.J., Brumberg, J.C., and Simons, D.J. (2000). Circuit dynamics and coding strategies in rodent somatosensory cortex. *J. Neurophysiol.* *83*, 1158–1166.
- Pinto, D.J., Hartings, J.A., Brumberg, J.C., and Simons, D.J. (2003). Cortical damping: analysis of thalamocortical response transformations in rodent barrel cortex. *Cereb. Cortex* *13*, 33–44.
- Poulet, J.F.a., Fernandez, L.M.J., Crochet, S., and Petersen, C.C.H. (2012). Thalamic control of cortical states. *Nat. Neurosci.* *15*, 370–372.
- Raimondo, J.V., Kay, L., Ellender, T.J., and Akerman, C.J. (2012). Optogenetic silencing strategies differ in their effects on inhibitory synaptic transmission. *Nat. Neurosci.* *15*, 1102–1104.
- Reinhold, K., Lien, A.D., and Scanziani, M. (2015). Distinct recurrent versus afferent dynamics in cortical visual processing. *Nat. Neurosci.* *18*, 1789–1797.
- Sederberg, A.J., Pala, A., Zheng, H.J.V., He, B.J., and Stanley, G.B. (2019). State-aware detection of sensory stimuli in the cortex of the awake mouse. *PLoS Comput. Biol.* *15*, e1006716.
- Sermet, B.S., Truschow, P., Feyerabend, M., Mayrhofer, J.M., Oram, T.B., Yizhar, O., Staiger, J.F., and Petersen, C.C.H. (2019). Pathway-, layer- and cell-type-specific thalamic input to mouse barrel cortex. *eLife* *8*, 1–28.
- Sherman, S.M. (2001a). A wake-up call from the thalamus. *Nat. Neurosci.* *4*, 344–346.
- Sherman, S.M. (2001b). Tonic and burst firing: dual modes of thalamocortical relay. *Trends Neurosci.* *24*, 122–126.
- Sherman, S.M. (2005). Thalamic relays and cortical functioning. *Prog. Brain Res.* *149*, 107–126.
- Sherman, S.M., and Guillery, R.W. (2002). The role of the thalamus in the flow of information to the cortex. *Philos. Trans. R. Soc. Lond. B Biol. Sci.* *357*, 1695–1708.
- Sherman, S.M., and Koch, C. (1986). The control of retinogeniculate transmission in the mammalian lateral geniculate nucleus. *Exp. Brain Res.* *63*, 1–20.
- Smith, G.D., Cox, C.L., Sherman, S.M., and Rinzel, J. (2000). Fourier analysis of sinusoidally driven thalamocortical relay neurons and a minimal integrate-and-fire-or-burst model. *J. Neurophysiol.* *83*, 588–610.
- Speed, A., Del Rosario, J., Burgess, C.P., and Haider, B. (2019). Cortical state fluctuations across layers of V1 during visual spatial perception. *Cell Rep.* *26*, 2868–2874.e3.
- Stanley, G.B., Jin, J., Wang, Y., Desbordes, G., Wang, Q., Black, M.J., and Alonso, J.-M. (2012). Visual orientation and directional selectivity through thalamic synchrony. *J. Neurosci.* *32*, 9073–9088.
- Steinmetz, N.A., Aydin, C., Lebedeva, A., Okun, M., Pachitariu, M., Bauza, M., Beau, M., Bhagat, J., Böhm, C., Broux, M., et al. (2021). Neuropixels 2.0: A miniaturized high-density probe for stable, long-term brain recordings. *Science* *372*, eabf4588.
- Stoelzel, C.R., Bereshpolova, Y., and Swadlow, H.A. (2009). Stability of thalamocortical synaptic transmission across awake brain states. *J. Neurosci.* *29*, 6851–6859.
- Stujenske, J.M., Spellman, T., and Gordon, J.A. (2015). Modeling the spatio-temporal dynamics of light and heat propagation for in vivo optogenetics. *Cell Rep.* *12*, 525–534.
- Suzuki, S., and Rogawski, M.A. (1989). Rogawski M a. *Proc. Natl. Acad. Sci. USA* *86*, 7228–7232.
- Swadlow, H.A. (2002). Thalamocortical control of feed-forward inhibition in awake somatosensory ‘barrel’ cortex. *Philos. Trans. R. Soc. Lond. B Biol. Sci.* *357*, 1717–1727.
- Swadlow, H.A., and Gusev, A.G. (2001). The impact of “bursting” thalamic impulses at a neocortical synapse. *Nat. Neurosci.* *4*, 402–408.

Urbain, N., Salin, P.A., Libourel, P.A., Comte, J.C., Gentet, L.J., and Petersen, C.C.H.H. (2015). Whisking-related changes in neuronal firing and membrane potential dynamics in the somatosensory thalamus of awake mice. *Cell Rep.* *13*, 647–656.

Wang, Q., Webber, R.M., and Stanley, G.B. (2010). Thalamic synchrony and the adaptive gating of information flow to cortex. *Nat. Neurosci.* *13*, 1534–1541.

Wehr, M.S., and Zador, A.M. (2003). Balanced inhibition underlies tuning and sharpens spike timing in auditory cortex. *Nature* *426*, 442–446.

Whitmire, C.J., Waiblinger, C., Schwarz, C., and Stanley, G.B. (2016). Information coding through adaptive gating of synchronized thalamic bursting. *Cell Rep.* *14*, 795–807.

Wilent, W.B., and Contreras, D. (2004). Synaptic responses to whisker deflections in rat barrel cortex as a function of cortical layer and stimulus intensity. *J. Neurosci.* *24*, 3985–3998.

Wilent, W.B., and Contreras, D. (2005). Dynamics of excitation and inhibition underlying stimulus selectivity in rat somatosensory cortex. *Nat. Neurosci.* *8*, 1364–1370.

Wright, N.C., Borden, P.Y., Liew, Y.J., Bolus, M.F., Stoy, W.M., Forest, C.R., and Stanley, G.B. (2021). Rapid cortical adaptation and the role of thalamic synchrony during wakefulness. *J. Neurosci.* *41*, 5421–5439.

Yang, H., Kwon, S.E., Severson, K.S., and O'Connor, D.H. (2016). Origins of choice-related activity in mouse somatosensory cortex. *Nat. Neurosci.* *19*, 127–134.

Yu, J., Gutnisky, D.A., Hires, S.A., and Svoboda, K. (2016). Layer 4 fast-spiking interneurons filter thalamocortical signals during active somatosensation. *Nat. Neurosci.* *19*, 1647–1657.

Yu, J., Hu, H., Agmon, A., and Svoboda, K. (2019). Recruitment of GABAergic interneurons in the barrel cortex during active tactile behavior. *Neuron* *104*, 412–427.e4.

Zhang, C., Yang, S., Flossmann, T., Gao, S., Witte, O.W., Nagel, G., Holthoff, K., and Kirmse, K. (2019). Optimized photo-stimulation of halorhodopsin for long-term neuronal inhibition. *BMC Biol.* *17*, 95.

STAR★METHODS

KEY RESOURCES TABLE

REAGENT or RESOURCE	SOURCE	IDENTIFIER
Bacterial and virus strains		
AAV-5-CamKinasell-eNph3.0	Gradinaru et al., 2010	Addgene, viral prep number 2966-AAV5
AAV-1-hsyn1-ArcLight	Jin et al., 2012	Addgene, plasmid number 36857
Deposited data		
Electrophysiology and imaging data	This paper	https://doi.org/10.5061/dryad.dbrv15f3n
Experimental models: Organisms/strains		
Mouse: C57BL/6J	N/A	Jackson Laboratory cat# 000664
Mouse: NR133	Gerfen et al., 2013	Jackson Laboratory
Software and algorithms		
Matlab	N/A	https://www.mathworks.com/products/matlab.html
Python 3.8.9	N/A	https://www.python.org/
KiloSort2	Steinmetz et al., 2021	https://github.com/MouseLand/Kilosort
Phy	N/A	https://github.com/cortex-lab/phy
Plexon Offline Spike Sorter	N/A	https://plexon.com/products/offline-sorter/
Analysis and modeling code	This paper	https://doi.org/10.5061/dryad.dbrv15f3n

RESOURCE AVAILABILITY

Lead contact

Further information and requests for data or code should be directed to and will be fulfilled by the lead contact, Garrett B. Stanley (garrett.stanley@bme.gatech.edu).

Materials availability

This study did not generate new unique reagents.

Data and code availability

- All data reported in this paper's figures have been deposited at Dryad and are available at the DOI listed in the [key resources table](#).
- All code for generating figures has been deposited at Dryad and is available at the DOI listed in the [key resources table](#).
- Any additional information required to reanalyze the data reported in this paper is available from the [lead contact](#) upon request.

EXPERIMENTAL MODEL AND SUBJECT DETAILS

All procedures were approved by the Institutional Animal Care and Use Committee at the Georgia Institute of Technology and were in agreement with guidelines established by the National Institutes of Health. Experiments were performed on adult (6–15 weeks) male and female Mice. Mice strains included C57BL/6J (Jackson Laboratories) and the transgenic NR133-Cre ([Gerfen et al., 2013](#)) on a C57BL/6J background mice.

METHOD DETAILS

AAV delivery

At least 5 weeks prior to experimentation, 6-week-old male and female C57BL/6J (Jackson Laboratories) mice were injected with different viral constructs either in the ventral posteromedial (VPM) thalamic region with AAV-5-CamKinasell-eNph3.0 (Addgene/UNC Viral Vector core) for optogenetic modulation, in the primary somatosensory (S1) cortex with AAV-1-hsyn1-ArcLight (Addgene/UPenn Viral Vector Core) for optical voltage imaging, or both. For surgical procedures, mice were anesthetized using isoflurane (3–5%). After the mouse was fully anesthetized, small craniotomies were placed over the regions of interest and were aligned using stereotaxic measurements (For VPM, 1.8mm lateral from midline by 1.8mm caudal from bregma). For cortical expression, either

single or multiple injection sites were used surrounding the barrel cortex (centered at 1.5mm caudal from bregma and 3mm lateral from midline). The virus was loaded into a modified Hamilton syringe (701-N) with a ~35 micron borosilicate glass pipette tip or a Hamilton Neuros Syringe. The syringe was initially lowered to the corresponding depth below the surface (for VPm: 3mm and For S1: 0.5mm) and the tissue was allowed to rest for 1 minute before injection. Both sites received injections of 0.5-1 μ l of viral construct at a flow rate of 0.1 μ l/minute. After injection, the pipette remained in place for an additional 5 minutes before slowly being removed from the brain. The bore holes were filled with either bone wax or left to close naturally. Throughout injection, mice were kept warm using a water heating system to maintain body temperature. See [Figure S1](#) for histological validation of expression of halorhodopsin in thalamus and ArcLight in S1.

Awake Animal Preparation

At least four weeks after ArcLight and eNphR3.0 viral injection, mice were anesthetized under isoflurane and were implanted with a head-plate. Over the course of 5-14 days preceding the first imaging experiment, mice were routinely handled to gain familiarity with the imaging system and immobilization device. During this acclimatization period, mice were head fixed for increasingly longer periods of time, from 15 minutes to 1.5 hours. During stimulation of the whisker, mice were prevented from interacting with the whisker stimulator by obstructing the path from the paws to the whisker. Mice were rewarded with sweetened milk (Nestle, Ltd.) throughout imaging. After at least 5 days of handling and acclimating, mice became tolerant to immobilization in the headplate restraint system. During passive stimulation of the whiskers, the mice often actively moved their whiskers. Therefore, the whisker stimulator was placed relatively close (5mm) to the face to prevent the whisker from slipping out of the manipulator; however, the amplitude of the deflection was adjusted to maintain a consistent angular velocity (1200 deg/s).

Whisker stimulation

Whisker stimulation was similar to that utilized previously ([Borden et al., 2017](#)). Briefly, individual vibrissae of the mice were deflected by a high fidelity (1 KHz) galvanometer system (Cambridge Technologies). A whisker stimulus was applied by positioning the custom designed galvanometer 5-10mm from the face and delivering an exponential sawtooth (rise and fall time = 5ms). The waveform stimulus velocity was taken by averaging the time to peak velocity of the stimulus. The velocity was adjusted based on distance from the face.

Thalamic and cortical electrophysiology

For thalamic electrophysiology, a small craniotomy was made over the primary whisker sensitive thalamic ventral-posterior medial (VPm) region of the mouse, around the injection site, using stereotactic coordinates (see above). VPm was then mapped under anesthesia using either a 2M Ω tungsten electrode (FHC) or 32-channel silicon probe (NeuroNexus Technologies). The mapping electrode was slowly lowered below the cortical surface during manual stimulation of the whiskers, while spiking activity (threshold crossings of high-pass filtered voltages) was monitored using the data acquisition system. We stopped descending when we recorded whisker-driven spiking activity at a depth consistent with VPm (typically 2900 – 3600 μ m below the surface). We then used the galvanometer to present precise single-whisker stimulation, and confirmed that multi-unit activity was consistent with electrophysiological features of VPm. Specifically, the electrode was determined to be located in VPm if the peri-stimulus time histogram (PSTH) contained a peak response 3ms - 10ms after a 1200 degree/s punctate single whisker stimulus and did not have a latency shift by more than 20ms after 1s of a 10Hz adapting stimulus ([Wang et al., 2010](#)). The principal whisker was determined by the largest 30ms PSTH response of multiple neighboring whiskers. We then noted the depth and stereotactic coordinates of this recording site and slowly retracted the mapping electrode, sealed the craniotomy, and returned the mouse to its home cage. During awake recording sessions, we targeted the same location for recording, briefly repeating the above steps to confirm electrode location. We recorded thalamic spiking using either a 2M Ω tungsten electrode (FHC) with 200 μ m attached optical fiber, or a 32-channel silicon probe array with 100 μ m attached optical fiber (A1x32-Poly3-5mm-25s-177-OA32LP, NeuroNexus Technologies). For cortical recordings, initial mapping was conducted using cortical ArcLight voltage imaging or intrinsic imaging (see below). Once the target cortical column (barrel) was identified and confirmed, a 32-channel linear silicon probe (A1x32-5mm-25-177, NeuroNexus Technologies) or single tungsten electrode (FHC) was inserted. For both thalamic and cortical electrophysiology, after the conclusion of the study either a small 7uA 10s lesion, or a fluorescent dye was placed near the recording location and confirmed using post-mortem histological validation. Neuronal signals were band-pass filtered (500Hz–5KHz), digitized at either 24.414 or 30 KHz/channel and collected using either a 96-channel (Blackrock Microsystems, Salt Lake City, UT, USA), or a 64-channel (Tucker-Davis Technologies, Alachua, FL, USA) data-acquisition system.

Awake cortical fluorescent arclight imaging

ArcLight transfected mice were imaged through the thinned or removed skull using a two-camera system: a Scimedica Imaging system to measure cortical ArcLight spatial activity, and a custom camera to measure hemodynamic activity for subtraction. The cortex was imaged using a 184 x123 pixel CCD Camera, MiCam2 HR Camera (Scimedica, Ltd) to capture ArcLight, and a Basler Ace (acA1920-155um) 480 x 180 pixel (4x4 binned) CMOS Camera to capture auto-fluorescence, at 200 Hz with a tandem lens microscope. The entire cortical area was illuminated at 465 nm with a 400 mW/cm² LED system (Scimedica, Ltd.) to excite the ArcLight fluorophore and background auto-fluorescence. The excitation light was projected onto the cortical surface using the first dichroic

mirror (bandpass: 475/625nm, Semrock, Inc.). Collected light was passed through a second dichroic mirror (Longpass cutoff: 495 nm, Semrock, Inc.) for collection of the ArcLight and auto-fluorescence signal. The auto-fluorescence signal was filtered with a bandpass filter between the wavelengths of 465/75 nm (Semrock, Inc). The ArcLight signal was filtered with a bandpass emission filter between wavelengths of 520/35 nm (Semrock, Inc.). The imaging system was focused approximately 300 μ m below the surface of the brain to target cortical layer 2/3, although the imaging likely captures fluorescence from the cell bodies as well as neuropil above and below layer 2/3.

Anesthetized cortical fluorescent arclight & intrinsic imaging

ArcLight transfected mice were imaged through the thinned or removed skull using a Scimedia Imaging system to measure cortical spatiotemporal activity (leveraging a single camera setup). The cortex was imaged using a 184x123 pixel CCD Camera, MiCam2 HR Camera (Scimedia, Ltd) at 200 Hz, and a tandem lens microscope. The entire cortical area was illuminated at 465 nm with a 400 mW/cm² LED system (Scimedia, Ltd.) to excite the ArcLight fluorophore. The excitation light was further filtered (cutoff: 472-430 nm bandpass filter, Semrock, Inc.) and projected onto the cortical surface using a dichroic mirror (cutoff: 495 nm, Semrock, Inc.). Collected light was filtered with a bandpass emission filter between wavelengths of 520-535 nm (Semrock, Inc.). The imaging system was focused approximately 300 μ m below the surface of the brain to target cortical layer 2/3. For intrinsic imaging of the hemodynamic response, the cortical surface was illuminated by a 625nm red LED (ThorLabs), and imaged with the same camera system as above, at a temporal resolution of 10Hz. During intrinsic imaging, no emission filters were used. In order to evoke a cortical intrinsic response, the whisker was repetitively stimulated at 10Hz for 6 seconds.

Functional fluorescent mapping of barrel cortex

The mouse's whisker system was first mapped by imaging the rapid ArcLight response to a high velocity (1200 Deg/s) sensory stimulus separately applied to three different whiskers. The resulting whisker response averaged over 20 trials was determined to be associated with a principal whisker, and barrel, if the evoked response was spatially limited to roughly a 0.2 mm x 0.2 mm area 25-30ms after stimulation. Additionally, the response was determined to be originating from the barrel field if the center of mass of activation moved consistently with the histologically defined barrel field and was within the standard stereotaxic location of S1 (~3mm lateral, 0.5-1.5mm from bregma). After mapping, a single whisker was deflected in a way as to emulate a high velocity slip-stick event (1200 deg/s), either with or without thalamic optogenetic hyperpolarization.

Simultaneous imaging and thalamic optogenetic manipulation

After mapping both the thalamic and cortical regions, an optrode (2M Ohm tungsten electrode mounted to a 200 μ m optic fiber) was positioned to the stereotaxic locations of the pre-mapped thalamic region and lowered to the corresponding depth. Once a single thalamic unit was identified using the above constraints, the unit was determined to be sensitive to optical stimulation by briefly (1-2s) hyperpolarizing the cells using ~17mW/mm² (LED condition) or ~35mW/mm (double LED condition) (unless otherwise noted) at 590nm from an LED light source (Thorlabs, M590-F1). Each cell was determined to be a thalamic optically sensitive unit if the light caused a transient decrease in firing rate or if the cessation of the 590nm light caused a rebound burst (Brecht and Sakmann, 2002). After identifying an optically sensitive thalamic unit, the whisker stimulus was presented under various light conditions. Light stimulation was presented 500-750ms preceding and following whisker deflection. There was at least a four second interval between stimulus deliveries to allow for recovery of halorhodopsin (eNphR3.0). Each session imaged 200ms-1s of frames preceding whisker stimulation to measure spontaneous activity. Prior to use, light power was measured from the tip of the ground optical fiber before each experiment to maintain approximate light intensities delivered to each cell. Although the in-vivo optogenetic implementation precludes precise knowledge of the degree of hyperpolarization of the thalamic neurons due to variations in opsin expression, position of optic fiber relative to cells, etc., a separate set of in-vitro, brain slice experiments showed that VPM neurons were hyperpolarized by ~15-25 mV for the light levels utilized (see Figure S2). Given that in the in-vitro experiments, light was presented more directly to the VPM neurons expressing halorhodopsin, and that in the in-vivo experiments the presentation of light did not completely silence the neurons, it is likely that the in-vitro experiments were an upper-bound for the in-vivo case, and the actual hyperpolarization induced in-vivo was less than that of the in-vitro experiments. During light delivery, the downstream cortical response was recorded using either electrodes for cortical electrophysiology or voltage imaging as described above. The optogenetic and viral expression of each experiment was verified through confocal and brightfield imaging of fixed slices.

The LED light intensity used for optogenetic stimulation is within the published range of light stimulation (35mW/mm² is estimated from our maximum power measure of ~1.1mW through a 200 μ m fiber) (Stujenske et al., 2015; Owen et al., 2019). Further, studies that have directly quantified the effects of optical stimulation on local tissue heating and neural activation (in the absence of opsin expression) have found no significant difference in the firing rate change for 1mW light intensity (Stujenske et al., 2015) or minor firing rate changes for 3mW light intensity, but no behavioral effects (Owen et al., 2019). See Figure S4 for controls that demonstrate a lack of light effects and lack of confounding interactions between optogenetic activation of VPM thalamus and GEVI imaging in cortical S1.

Anesthetized electrophysiology

A subset of experiments was conducted with mice under light anesthesia, as a control. These mice were initially anesthetized using isoflurane (3-5%) and then placed on a heated platform (FHC, Inc.) in a stereotaxic nose cone to maintain anesthesia. A large incision

was placed over the animal's skull, and the connective tissue and muscle surrounding the skull was removed using a fine scalpel blade. A modified headplate was attached using dental acrylic (Metabond) and secured to the skull. For cortical imaging, the skull was thinned with a dental drill until transparent, or removed entirely and covered with saline or ringers' solution. After surgery, the isoflurane levels were dropped to $\sim <1\%$ for imaging and electrophysiology, the procedures for which were identical to those for the awake animal. The animal's vitals (heart rate and respiratory rate) were constantly measured for tracking anesthesia depth.

Histology

Histological procedures were similar to those utilized previously (Borden et al., 2017), to validate ArcLight in S1 and/or opsin expression in VPM thalamus. Histological samples were prepared by perfusing the animal transcardially with phosphate buffered saline (PBS) followed by 4% paraformaldehyde. Brains were post-fixed overnight in 4% paraformaldehyde then transferred to PBS before sectioning. Thick sections were cut using a vibratome (100 μm , Leica, VTS 1000) and either directly mounted or saved for staining. See Figure S1 for histological validation of expression of halorhodopsin in VPM and ArcLight expression in cortex.

Integrate & Fire or Burst (IFB) Modeling

To further explore the surprising finding of relatively invariant baseline firing rates during hyperpolarization of VPM thalamus, we utilized a biophysically inspired model of thalamic burst/tonic firing. Specifically, we suggest that this finding was a consequence of the burst mechanism, and not the result of possible confounds related to previously reported changes in reversal potential of chloride during prolonged periods of halorhodopsin activation (Raimondo et al., 2012). The Integrate and Fire or Burst (IFB) model was derived from previously published models of thalamic function from the LGN (Smith et al., 2000; Lesica and Stanley, 2004; Lesica et al., 2006). In order to simulate the experimental parameters and account for changes in thalamic activity, some additional terms and parameters were added and adjusted. Additionally, we generated ongoing activity using two methods, either injected current noise or synaptic events, with both showing the same results. The results shown here use the synaptic event model where IPSCs and EPSCs are modulated as fixed inputs. The model itself was written and analyzed using custom scripts in Matlab 2016a.

The model is based on modifications of the standard integrate and fire model representing the effects of integrated synaptic currents on membrane voltage:

$$C \frac{dV}{dt} = I_{EPSC} - I_{IPSC} - I_L - I_T - I_{Halo}$$

$$I_L = g_L(V - V_L), I_T = g_T m_{\infty} h(V - V_T)$$

$$\frac{dh}{dt} = \begin{cases} \frac{-h}{\tau_h^-}, & (V > V_h) \\ \frac{(1-h)}{\tau_h^+}, & (V < V_h) \end{cases}$$

$$\frac{dI_{EPSC}}{dt} = \frac{I_{EPSC}}{\tau_s}$$

$$\frac{dI_{IPSC}}{dt} = \frac{I_{IPSC}}{\tau_s}$$

The following parameters were used to simulate thalamic activity: $C = 2\text{uF}/\text{cm}^2$, $g_L = 0.035\text{ mS}/\text{cm}^2$, $g_T = 0.07\text{ mS}/\text{cm}^2$, $V_L = -65\text{mV}$, $V_{reset} = -45\text{mV}$, $V_h = -68\text{mV}$, $V_T = 120\text{mV}$, $\tau_h^+ = 0.1\text{s}$, $\tau_h^- = 0.02\text{s}$, $\tau_s = 1\text{e} - 2\text{uF}/\text{cm}^2$, $Threshold = -35\text{mV}$, $I_{Halo} = 0 - 1\text{uA}/\text{cm}^2$. EPSPs occurred at a rate $EPSP_{rate} = 1 - 25\text{Hz}$, where each excitatory post-synaptic event had a peak of $3\text{nA}/\text{cm}^2$, and decayed according to the above first-order differential equation for I_{EPSC} . Similarly, IPSPs occurred at a rate of $IPSP_{rate} = 0 - 5\text{Hz}$, where each inhibitory post-synaptic event had a peak of $1\text{uA}/\text{cm}^2$, and decayed according to the above first-order differential equation for I_{IPSC} . To simulate the different levels of thalamic activity, we varied the rates of EPSP inputs on the thalamic model (based on published ranges of thalamic activity (Urbain et al., 2015)). IPSPs were simulated at a much lower rate (20% of EPSP rate) to add additional variability to baseline activity. The model outputs represent the average response of 100 simulated thalamic neurons in response to various levels of thalamic hyperpolarization and baseline activity. The model was updated at 1ms steps. The absolute refractory period was set to 1ms.

Cortical E-I modeling

We constructed a simple model of the thalamocortical network using custom scripts written in Python 3.6.10, as described (Wright et al., 2021). We modeled a single cortical barrel as a clustered network of excitatory and inhibitory single-compartment leaky integrate-and-fire (LIF) neurons, subject to excitatory thalamic and non-thalamic synaptic inputs. For each condition, we simulated 50 trials (200 ms per trial), with a time-step of 0.05 ms. This network mimics the numerical expansion of neurons at the thalamocortical

junction, and incorporates several known properties of thalamocortical and intracortical connectivity. We previously tuned model parameters to produce qualitatively realistic velocity tuning curves (Wright et al., 2021), and adopted those same parameters here.

Model of VPM barreloid

We modeled a single VPM barreloid as forty independent spike trains. The grand mean pre-stimulus firing rate was set equal to the empirical grand-mean VPM rate in a 30 ms pre-stimulus window for each condition (9.14 Hz for control and 7.34 Hz for LED, calculated from the 46 sensory-responsive VPM units recorded via silicon probe). The ongoing and evoked rates for each neuron were then multiplied by a rate modulation factor drawn from a skewed gamma distribution (with a shape value of 2.0, a scale value of 1.0, then re-scaled to have a mean value of 1.0), to mimic the broad firing rate distributions of VPM neurons previously reported (Pinto et al., 2000; Bruno and Simons, 2002; Wang et al., 2010; Whitmire et al., 2016). Tonic and burst spike times for a given neuron were then drawn from their associated empirical PSTHs, and multiplied by the neuron's rate factor. For tonic spikes, we required a minimum inter-spike interval (ISI) of 4 ms for all spikes drawn for a given neuron and trial. We modeled bursts as triplets of spikes: we first drew one spike time from the empirical burst PSTH, and then added spikes 1.25 ms before and after this central spike. We further required at least 2 ms of silence before the first spike in each burst, and excluded any bursts with spike times that fell outside of the trial window. Model VPM neurons were independent, in that spike times for each neuron were drawn independently. In this standard model, we did not make any additional assumptions regarding evoked VPM synchrony in the control and LED conditions, but by construction this resulted in across-condition synchrony effects that were consistent with the experimental observations. In our alternate models, we manually manipulated the rate of synchronous tonic spiking across VPM spike trains, while holding the rate of tonic and burst spikes fixed. Specifically, for each sensory-evoked tonic VPM spike that occurred within ± 5 ms of the VPM tonic PSTH peak, we moved the spike away from the PSTH peak with probability P (repeating this simulation for $P = 0.05, 0.15, 0.25$). The new spike time was the grand PSTH peak time plus a random value. To obtain this random value, we first drew a spike time from a normal distribution with zero mean and standard deviation of 20 ms, took the absolute value, and added 5 ms.

Thalamocortical connectivity

Non-zero thalamocortical (TC) synaptic weights were broadly distributed, and we implemented differential TC connectivity by imposing higher TC convergence (Bruno and Simons, 2002; Cruikshank et al., 2007) and shorter synaptic latencies (Cruikshank et al., 2007; Kimura et al., 2010) for inhibitory neurons, and requiring that VPM neurons with the highest mean rates synapsed only onto inhibitory neurons (Bruno and Simons, 2002). Because we sought to investigate the effects of changes in synchronous thalamic spiking and single-neuron bursting on downstream network activity, we did not impose activity-dependent depression at the TC synapse. Given the very short intervals between burst spikes, the relatively slow recovery of a given thalamocortical synapse following the first spike in a burst would in principle diminish the efficacy with which subsequent spikes in the burst drive postsynaptic targets. Yet we show here that this consideration is not required to match experimental observations.

Each VPM neuron synapsed onto a subset of cortical network neurons via a set of thalamocortical (TC) synapses, with at most one synapse between each VPM and each network neuron. As done previously (Wright et al., 2021), we implemented differential TC connectivity by setting higher TC synaptic convergence (Bruno and Simons, 2002; Cruikshank et al., 2007) and shorter synaptic latencies (Cruikshank et al., 2007; Kimura et al., 2010) for inhibitory than for excitatory neurons, and also by requiring that VPM neurons with the highest firing rates synapse exclusively onto inhibitory neurons (Bruno and Simons, 2002), which generally supported strong feedforward inhibition in this model network.

Each thalamic spike resulted in a postsynaptic conductance in each postsynaptic cortical neuron, and we tuned the TC synaptic conductance amplitude such that near-simultaneous firing of multiple thalamic neurons was required to evoke action potentials in target neurons (Bruno and Sakmann, 2006) when intracortical synaptic strengths were set to zero.

Model of S1 network

We modeled a single cortical column as a network of 800 excitatory and 100 inhibitory LIF neurons with "small-world" connectivity, as described previously (Wright et al., 2021). We tuned network connectivity parameters such that thalamic and random external inputs together could evoke bouts of persistent network firing on a given trial, but without runaway firing. For network LIF neurons, we selected intrinsic excitatory and inhibitory neuronal properties that were consistent with previous modeling studies, and/or were motivated by previous experimental work, as described previously (Wright et al., 2021). Generally, inhibitory neurons had shorter membrane time constants and refractory periods than excitatory neurons, and excitatory neurons were subject to spike-rate adaptation.

For each condition, we simulated 50 trials, each lasting 200 ms (including a 50 ms "buffer window" to allow the network to reach steady-state, a 50 ms "pre-stimulus" window, and a 100 ms "post-stimulus" window), with a time-step of 0.05 ms. At each time-step, the membrane potential V of a given network neuron evolved according to its synaptic inputs, as described previously (Wright et al., 2021).

We employed alternate models to parse the roles played by changes in thalamic bursting per se, and by changes in synchronous thalamic spiking. In these alternate models, we manually manipulated tonic spike times to effect changes in the rate of synchronous

tonic input spikes, while holding mean tonic and burst rates fixed. Specifically, for each trial and spike train, we probabilistically relocated tonic spikes that occurred within ± 5 ms of the early PSTH peak to a later (random) time within approximately the first 30 ms post-stimulus.

For each model, we calculated the grand mean \pm SEM firing rates for all neurons, for an “early” (0 – 30 ms post-stimulus) and “late” (60 – 100 ms post-stimulus) response window, where stimulus onset time represents the time of galvo deflection onset, or $t = 0$ in the empirical VPM PSTH. For cortical network synchrony analysis, we randomly selected 200 excitatory and 200 inhibitory neuron pairs. We then calculated synchrony for each “valid” pair, i.e., each of these pairs with at least one relative spike time in the 30 ms post-stimulus window across all trials. For the VPM spike train synchrony analysis, we randomly selected 50 VPM neuron pairs, and repeated the procedure described above for the experimental VPM data. Note that we used this calculation to confirm that drawing thalamic spike times from the empirical VPM PSTHs, and assuming independence across these input spike trains, was sufficient to reproduce the empirical trends in synchronous thalamic spiking.

QUANTIFICATION AND STATISTICAL ANALYSIS

Thalamic electrophysiology data analysis - Mean response, burst ratio, synchronous spike counts

We report several different basic measurements of spiking activity from our thalamic units including evoked response and evoked bursting response. Thalamic firing activity was reported as PSTHs with units of firing rate in Hz, calculated as the number of spikes within a bin, divided by the size of the bin (see individual plots for bin size). We determined thalamic evoked response as the initial response (0-30ms) to sensory stimuli, reported as the number of spikes per stimulus averaged over many trials (9-102 trials). The corresponding evoked bursting response was determined as the number of bursting spikes per trial in that same post stimulus period. Bursting spikes were defined as 2 or more spikes that fire at most 4ms apart preceded by 100ms of silence. The 100ms pre-stimulus activity is based on reported values for T-type calcium bursts (Lu et al., 1992; Swadlow and Gusev, 2001; Whitmire et al., 2016). All data analysis of the recorded extracellular thalamic units was accomplished using custom Matlab and Python scripts.

We calculated the mean synchronous spike counts using all pairs of sensory-responsive thalamic neurons recorded simultaneously using silicon probes, as described previously (Wright et al., 2021). Briefly, for each pair of simultaneously recorded, sensory-responsive single-units, we considered the spike times in a brief (10 ms) post-stimulus window, and calculated the relative spike times (which ranged from +20 ms to -20 ms). We repeated this for all pairs, populating a grand set of relative spike times, separately for each light level, generating the spike cross-correlogram (CCG). We then summed the CCG between +5 ms and -5 ms, and divided by the number of contributing pairs. We repeated these steps using an equivalent number of random relative spike times, and subtracted the synchronous spike counts for these shuffled relative spike times from the true synchronous count. This yielded the “mean synchronous spike count (shuffle-corrected)”, or the average number of synchronous spike counts per pair, beyond what would be predicted from pairs of neurons with randomized relative spike times. We calculated 95% confidence intervals by re-sampling the relative spike times with replacement. We performed this analysis for three separate windows: 0 – 10 ms, 10 – 20 ms, and 20 – 30 ms post-stimulus.

Thalamic and cortical electrophysiology data analysis

Offline spike sorting was accomplished using either the Plexon Offline Spike Sorter v4 (Plexon, Inc, for tungsten electrode thalamic recordings), or KiloSort2 (Steinmetz et al., 2021), followed by curation in Phy (for silicon probe recordings in thalamus and cortex). We then required each unit to satisfy various criteria in order to be considered a well-isolated single-unit. We first calculated the signal-to-noise ratio (SNR), or the amplitude of the mean waveform (trough-to-peak) divided by the standard deviation. Second, we calculated the inter-spike-interval (ISI) violation percentage, or the percentage of all spikes within the 0 – 1 ms inter-spike interval. We required the SNR to be greater than or equal to 2 (3), and the ISI violation percentage to be less than or equal to 1 (1.5) for cortex (thalamus). Cortical single-units were classified as putative Regular Spiking Units (RSUs) or Fast Spiking Units (FSUs) based on the characteristics of the spike waveform (McCormick et al., 1985; Niell and Stryker, 2010; Guo et al., 2017; Speed et al., 2019; Yu et al., 2019). Specifically, units with a spike-width exceeding 0.4 ms (defined as trough-to-peak) were classified as RSUs, and below this as FSUs. For thalamic single-units, we required the spike-width to exceed 0.3 ms, as narrower waveforms could reflect activity at TRN synaptic terminals (Barthó et al., 2014). For multi-unit data, we measured threshold crossings from the continuously recorded thalamic or cortical activity. Thalamic multiunit activity was captured using a threshold criterion of 5 standard deviations over the entire recording (Yang et al., 2016). For cortical multiunit recordings, a manual threshold was set based on each experiment. Additional data analysis utilized custom scripts using Matlab (Mathworks, Inc).

Cortical units were initially analyzed together, across recording sites, as the dataset was not sufficient to confidently assess any cross-laminar effects. However, we did repeat some analyses using only putative layer 4 (L4) units, identified using methods similar to those described previously (Sederberg et al., 2019), as L4 was particularly important to this study as the primary thalamorecipient cortical layer. Briefly, for each experiment, we first calculated the across-trial average local field potential (LFP, or 2 – 200 Hz band-pass-filtered voltage traces) and multi-unit (MU, threshold crossings of 150 Hz highpass-filtered voltage traces) responses to punctate whisker deflections. We then calculated the current source density (CSD) profile of the LFP responses. Finally, we used a combination of the amplitudes and latencies of LFP deflections, the locations and latencies of CSD sinks, the amplitudes and latencies of MU firing, and the approximate probe depth to estimate the center of L4. Specifically, L4 is expected to be 400 – 600 μm

below the cortical surface, and exhibit short-latency, large-amplitude LFP and MU responses, and a short-latency CSD sink. We required at least two of the three electrophysiological signals (LFP, CSD, MU) to provide qualitative agreement on the L4 center, and for this center to be between 400 and 600 μm below the estimated cortical surface, which excluded one of the six experiments from this analysis. Finally, we considered L4 channels to be those between 100 μm above and 100 μm below the central channel. A cortical single-unit was deemed a putative L4 unit if the channel on which its mean waveform was largest was included in the list of putative L4 channels.

Cortical firing activity was reported as PSTHs with units of firing rate in Hz, calculated as the number of spikes within a bin, divided by the size of the bin (see individual plots for bin size). All cortical spikes within a 1ms ISI were removed from analysis (and this was $<1\%$ of total). Synchrony across cortical single-units was computed from spike cross-correlograms across recorded pairs. Specifically, synchrony was defined as proportion of spikes from the full ($\pm 100\text{ms}$) cross-correlogram that were in a central $\pm 7.5\text{ms}$ window (Wang et al., 2010; Whitmire et al., 2016). To determine the number of needed synchronous events to accurately measure synchrony, we simulated two neurons with a $\sim 5\%$ change in synchrony (assuming a normal distribution). We found that approximately 50 events were required to accurately separate the two distributions.

Voltage imaging data processing

Raw images were loaded and converted from the SciMedia “.gsd” format using custom scripts and down-sampled by a factor of two. Each dataset was first normalized to a $\% \Delta F/F_0$ measurement by subtracting and dividing each trial by the temporal average of the frames 0 to 200ms preceding light delivery (F_0). Note that throughout the analyses, the negative of the change in fluorescence is reported so that an increase in neural activity corresponds to a positive increase in the fluorescence measure. In two instances, where 200ms of preceding LED onset activity was not captured, the F_0 was taken as an average 200ms period across no-stimulus trials. Hemodynamic noise was removed using a PCA background subtraction method. As described in detail (Borden et al., 2017), *in vivo* ArcLight imaging overlaps with the hemoglobin absorption spectrum, and therefore contains hemodynamic noise that must be removed for analysis. Imaging the wildtype mouse cortical surface using the same blue excitation and ArcLight filter set revealed similar patterns of oscillatory activity, likely through auto-fluorescence and effects of hemodynamic absorption and blood flow (Ma et al., 2016). The background PCA subtraction utilizes the auto-fluorescence signal from non-ArcLight transfected regions to predict the hemodynamic signal across the recorded space. Specifically, the method uses principal component analysis of non-expressing low background auto-fluorescence regions (determined from the maximum fluorescence from a non-injected animal) to find the ongoing hemodynamic components on a single trial basis. Additionally, the background fluorescence regions were selected at least 1mm away from the recorded whisker evoked response (Borden et al., 2017). Ideally, these criteria would create a spatially defined region with little or no ArcLight fluorescence to isolate the hemodynamic signal from the signal of interest. Each frame is first spatially averaged by either a 200 μm x 200 μm circular averaging (pillbox) filter or a media filter to reduce noise. On a single trial, the corresponding top five principal components of the low background regions (which contains approximately 85% of the variance explained) are projected on a pixel-by-pixel basis across the entire recording using a lasso regression method with regularization. The lasso regression utilizes a cross-validated approach to determine the minimum number of components to develop the model of hemodynamic noise. In order to prevent the removal of any stimulus evoked activity, each pixel was fit on pre-stimulus activity (either before light onset for experiments involving optogenetics, or immediately preceding stimulus delivery). The final predicted hemodynamic signal for each pixel was subtracted across the entire recording on a pixel-by-pixel basis. Due to the complex waveform of the hemodynamic response, a simple notch filter is not effective at separating the signal from the noise (Borden et al., 2017). We found that the background PCA subtraction method greatly reduced hemodynamic signal across the entire frame, compared to the off-ROI method (Borden et al., 2017). In some instances, brief onset and offset light artifacts of the 590nm light was visible in the recorded ArcLight cortical signal. To account for any optogenetic transient light artifacts, we only considered the relative changes in fluorescence during steady state light levels. Both raw and processed images showed qualitatively similar results.

Awake voltage imaging data analysis – Dual camera

In the awake animal, we utilized a dual camera imaging system to capture a background fluorescence signal for hemodynamic subtraction. Two different cameras were used to capture the ArcLight and auto-fluorescence signals, and therefore, pixels could not be directly registered for subtraction for pixel-by-pixel correction. Instead, we utilized the same Background PCA subtraction method to find and develop models of the hemodynamic response based on the global PCA signal derived from the background image. For the dual camera data, each component was fit over the entire recording for subtraction of the hemodynamic noise. Both raw and processed images showed qualitatively similar results. Unless otherwise noted, each dataset was processed with the Background PCA or Dual Camera subtraction method as stated above.

Imaging data analysis – Peak amplitude, normalized peak, and temporal properties

We measured the effect of the optogenetic stimulation on the peak amplitude of the evoked mean ArcLight fluorescence in the determined cortical barrel. The cortical barrel region of interest (ROI) for each stimulated barrel and each data set was selected as the $\sim 200 \mu\text{m}$ x 200 μm region with the largest response 30ms after stimulus delivery. This determined ROI was used for all subsequent analyses of the temporal response. To better isolate the evoked amplitude, the frame preceding stimulus delivery ($t = -5\text{ms}$) was subtracted from the resulting recorded signal. For each recording, the peak amplitude was defined as the $\Delta F/F_0$ at the time of the

maximum average response between 0 and 110ms for the strongest stimuli (1200 Deg/s) presented under control and various opto-genetic conditions. Note that the convention used throughout the analyses here is to present the negative of the fluorescence measure, such that an increase in neural activity corresponds to a positive change in the fluorescence measure. In order to measure the temporal properties of the evoked response, we concentrated on the timeseries data from the determined cortical barrel ROI. For normalized fluorescence ($\text{Norm } \Delta F / F_0$), each session's peak response was divided by the average peak response to the strongest stimulus (1200 Deg/s) under the control condition. The normalization allows for a better comparison across animals which may have different levels of ArcLight expression. Peak time was defined as the time of the maximum fluorescence between 0 and 110 ms post stimulus, and the time of return to baseline as the time when the fluorescence crossed the pre-stimulus baseline value following the peak. Peak-to-baseline was then calculated as the time between the fluorescence peak and the return of the fluorescence to baseline. Recovery was defined as the average fluorescence in the 120-400ms window following the stimulus.

Imaging data analysis – Area measurements

In addition to measuring the peak response, we also measured the effect of different thalamic states on the evoked area of sensory cortical activity. We measured the activated area as the number of pixels exceeding a threshold using the average response at the peak frame (0-110ms) preceding stimulus delivery. Similar to other studies (Lustig et al., 2013; Millard et al., 2015), we measured the spatial activation using the 70% threshold. To compare the area independent of amplitude changes, we normalized the peak frame by dividing by the peak fluorescence in each condition (Control and LED). In order to isolate the evoked activity from ongoing activity, we subtracted the frame preceding stimulus delivery ($t=-5\text{ms}$). Different thresholds had no effect on the observed trends.

Statistical analysis

All tests were conducted using the MATLAB Statistics Toolbox (Mathworks, Inc.). For all measurements, we determined if the specific data sets were normally distributed using the Lilliefors test for normality. If the data were normal, we used the appropriate (paired or unpaired) t-test for statistical difference. If the population was determined to have non-normal distributions, we conducted non-parametric Wilcoxon signed-rank tests to determine statistical significance. All sample sizes are reported in the Fig. captions, along with an indication of particular test and the corresponding statistical significance level (* - $p<0.05$, ** - $p<0.01$, *** - $p<0.001$ in figures).